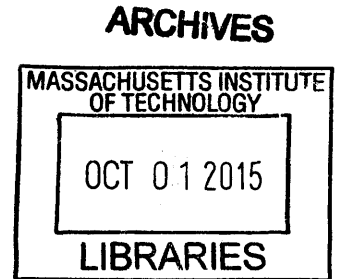


Small-Scale Advanced Thermo-Adsorptive Battery Prototype

by

Ari S. Umans

S.B. Department of Mechanical Engineering
Massachusetts Institute of Technology, 2013



Submitted to the Department of Mechanical Engineering in Partial Fulfillment of the
Requirements for the Degree of

MASTER OF SCIENCE IN MECHANICAL ENGINEERING

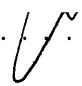
AT THE

MASSACHUSETTS INSTITUTE OF TECHNOLOGY

September 2015

© 2015 Massachusetts Institute of Technology
All rights reserved.


Signature redacted

Signature of Author 

Department of Mechanical Engineering

August 20, 2015


Signature redacted

Certified by 

Evelyn N. Wang

Associate Professor of Mechanical Engineering

Thesis Supervisor


Signature redacted

Accepted by 

David E. Hardt

Professor of Mechanical Engineering

Chairman, Department Committee on Graduate Students

Small-Scale Advanced Thermo-Adsorptive Battery Prototype

by

Ari S. Umans

Submitted to the Department of Mechanical Engineering on August 20, 2015, in Partial Fulfillment of the Requirements for the Degree of Master of Science

Abstract

A significant effort is underway to develop an adsorption-driven system with the capacity to replace the heating, ventilation and air-conditioning (HVAC) system in an electric vehicle. This Advanced Thermo-Adsorptive Battery (ATB) system uses novel adsorbent materials and methods of optimizing transport properties, without which the desired energy and power densities are unattainable. The work in this thesis runs parallel to that effort, with the development of a small-scale version of the ATB. Two novel prototype designs are discussed. The first, though never fully operational, was an attempt to demonstrate the potential of ATB technology to be scaled to meet countless heating and cooling applications. The second prototype was designed to be a system for testing aspects of ATB operation on a small scale. This prototype uses small quantities of adsorbents, reducing material costs and shortening time scales, and has a great deal of operating flexibility, enabling a number of system conditions to be parametrically studied. Testing and experimental procedures have been developed, and preliminary experimental data have been used to ensure proper prototype operation. This prototype will continue to be used as a tool to characterize ATB system operation and aid in understanding the technology.

Thesis Supervisor: Evclyn N. Wang

Title: Associate Professor of Mechanical Engineering

Acknowledgments

I would first like to thank my advisor, Prof. Evelyn Wang, for finding such an enjoyable project for me and guiding me through it. Next I must acknowledge the tremendous amount of help and wisdom received from Shankar Narayanan, who led the project so well and will continue to do so with future projects at RPI. It was truly a pleasure working with the ATB team at MIT, namely Hyunho Kim, Dr. Sungwoo Yang, Dr. Xiansen Li, Dr. Sameer Rao, Ian McKay, and Dr. Scott Schiffres, our collaborators at Northeastern, Prof. Carlos Hidrovo, Dr. Carlos Rios, and Arjun Venkataramanan, and Mike Levin at Ford. Special thanks to Carlos Jimenez for his help wrapping up this work and for the work he and Josh Acosta will continue as the project progresses. Thanks to the members of the Device Research Lab for creating such a great community to work in. I would like to thank the Advanced Research Projects Agency - Energy (ARPA-E) for funding this work and for their help in shaping the direction of the project. Lastly, thanks to my family for their support, with added thanks to my father for his help with writing and editing.

Contents

1	Introduction	9
2	Background	11
2.1	Advanced Thermo-Adsorptive Battery Operation	11
2.2	Adsorbents	12
2.2.1	Adsorption Isotherms	13
2.2.2	Heat of Adsorption and Adsorption Energy	15
2.3	Previous Small-Scale Prototype Work	16
2.4	Small-Scale ATB Prototype Objectives	18
2.4.1	Button Cell Prototype Objectives	18
2.4.2	Dual Chamber Prototype Objectives	18
2.5	Small-Scale ATB Concepts	19
2.5.1	Button Cell Prototype	19
2.5.2	Dual Chamber Prototype	22
3	Button Cell Prototype	26
3.1	Button Cell Prototype Design	26
3.2	Manufacturing Challenges	28
3.2.1	Design Restrictions	28
3.2.2	Bonding Differing Materials	28
4	Dual Chamber Prototype	32
4.1	Dual Chamber Prototype Design	32
4.2	Dual Chamber Operating Modes	38
4.2.1	Preconditioning	38
4.2.2	Leak Testing and Sensor Check	40

4.2.3	Desorption Mode	41
4.2.4	Adsorption Mode	43
5	Testing of the Dual Chamber Prototype	44
5.1	Predicted Performance	44
5.1.1	Zeolite MgY Sample	44
5.2	Test Results	46
5.2.1	Experiments With Over-filled Reservoir	46
5.2.2	Experiments With Under-filled Reservoir	50
5.2.3	Experiments With Refilled Reservoir	52
5.2.4	MgY Sample Degradation	53
6	Conclusions & Future Work	55

List of Figures

1	Pressure vs. temperature for ATB operation cycle	11
2	ATB operation schematic	12
3	Aluminosilicate zeolite structure	13
4	Representative Type I isotherm	14
5	First small-scale ATB prototype	17
6	Button Cell Prototype configuration schematic	19
7	Button Cell Prototype operation	21
8	Dual Chamber Prototype configuration schematic	22
9	Dual Chamber Prototype adsorption operation	23
10	Dual Chamber Prototype desorption operation	24
11	Button Cell Prototype CAD model	26
12	Button Cell Prototype exploded CAD model	27
13	Steel electroplating and soldering process	29
14	Soldering setup	29
15	Picture of two Button Cell Prototypes	30
16	Dual Chamber CAD model	32
17	Picture of the Dual Chamber Prototype in the lab	33
18	Internal chamber components	33
19	Chamber construction	34
20	Dual Chamber Prototype testing schematic	35
21	Heat-flux sensor attachment	35
22	Modified heat flux sensor attachment	36
23	Chiller plate	37
24	Dual Chamber Prototype with insulation and heaters	37
25	Filling station schematic	39

26	Dual Chamber Prototype reservoir on filling station	40
27	Dual Chamber Prototype testing schematic (copy)	41
28	Adsorbent chamber insulation	42
29	MgY sample	44
30	MgY Isotherm	45
31	Dual Chamber Prototype early stage design	46
32	Over-filled reservoir typical desorption temperatures	47
33	Over-filled reservoir typical adsorption temperatures	48
34	Over-filled reservoir typical adsorption powers and energies	48
35	Adsorption temperatures with cooling in adsorbent tube	49
36	Desorption with condensation plot of temperatures	50
37	Condensation power and energy	51
38	Tests 4 and 16 desorption conditions	52
39	Test 16 adsorption heating and cooling powers and energies	53

List of Tables

1	Comparison of tests 4 and 16	53
2	Desorption test temperature ramping rates	54

1 Introduction

This work demonstrates the use of adsorbent materials as the driving source of heating and cooling power in a portable prototype. Integration of an adsorption bed, evaporator/condenser, and reservoir into a single vacuum-sealed enclosure enables the production of simultaneous heating and cooling of separate surfaces at the turn of a valve. An adsorption heating/cooling system operates under saturated liquid/vapor conditions, using the adsorption bed to adsorb vapor, releasing heat and reducing the internal pressure. The pressure drop drives evaporation, cooling the evaporator and reducing the quantity of liquid in the reservoir. This process can be reversed by inputting heat to the adsorption bed, causing desorption of vapor which is condensed at the condenser and refills the reservoir.

The objective of this work was to design and manufacture an operational adsorption-based heating and cooling system using a novel MgY zeolite developed for high performance applications [1]. This new material gave rise to whole new opportunities for adsorption systems, since its high water uptake and high heat of adsorption enable exceptionally high heating and cooling energy densities. Work is currently underway to produce an adsorption climate control system, known as an Advanced Thermo-Adsorptive Battery (ATB), for electric vehicles (EVs) using MgY zeolite [2, 3]. To aid that work, the idea for a small-scale proof of concept ATB prototype was devised, aiming to demonstrate the operation of the ATB [4].

A small-scale prototype was developed for this purpose and several experiments were conducted to characterize its components [4]. This prototype had several design issues that indicated that a smaller, all-metal prototype would be able to take the work forward. This is the starting point for the work discussed in this thesis.

To begin this effort, a Button Cell Prototype ATB was designed and fabricated. The Button Cell was a compact version of the larger EV climate control system, with a volume on the order of 1/1000 times the size. Challenges in manufacturing, specific to building such a compact prototype, prevented this system from operating as desired, yet the process of building it helped guide the design of the large system.

To further aid the system effort, a second prototype, referred to as the Dual Chamber Prototype for its two distinct chamber components, was designed with different objectives than the Button Cell Prototype. This prototype was more focused on the understanding of how the system works with the goal of being a testing system for different operating conditions. The knowledge gained from the Button Cell Prototype effort led to a simpler, more robust design, which has been used to run experiments with an MgY zeolite adsorbent sample.

This thesis proceeds in the following fashion. Section 2 provides a quick description of ATB operation, an overview of adsorbent materials, and a discussion of the first small-scale ATB prototype. Also in Sect. 2 are the goals for each of the two new prototypes and descriptions of how these prototypes use adsorbents to generate heating and cooling

energies. Section 3 discusses the design of the Button Cell Prototype and the challenges in its construction that ultimately led to the abandonment of its design in favor of the simpler Dual Chamber Prototype. This prototype design is explained in Sect. 4, along with detailed descriptions of its modes of testing. Section 5 contains theoretical performance predictions and discussion of the sets of experiments that were used to troubleshoot the prototype and optimize its design. Conclusions and suggestions for future work are addressed in Sect. 6.

2 Background

2.1 Advanced Thermo-Adsorptive Battery Operation

The Advanced Thermo-Adsorptive Battery (ATB) concept was conceived as a means to replace the heating, ventilation, and air-conditioning (HVAC) system in an electric vehicle (EV) [2, 3]. The system uses four main components - reservoir, evaporator, adsorption bed, and condenser - to generate adsorptive heating and evaporative cooling energies. This process is carried out by evaporating an adsorbate, which begins as liquid inside the reservoir, and allowing the vapor to adsorb into the adsorption bed. This can be reversed with an input of energy, recharging the system by returning it to its starting configuration. The energy input desorbs adsorbate from the adsorption bed and condenses it, returning it to the reservoir as liquid.

Figure 1 depicts a pressure vs. temperature cycle at the adsorption bed, consisting of both the adsorption and desorption processes (d-a and b-c respectively) in addition to the sensible heating processes of operation (c-d and a-b). Processes c-d and d-a collectively make up system discharge, releasing heat energies Q_{cd} and Q_{da} , and a-b and b-c make up system recharge, consuming heats Q_{ab} and Q_{bc} .

A schematic of the ATB process in its discharging (energy generating) mode can be seen in Fig. 2(a) and in its recharging (energy consuming) mode in Fig. 2(b). The solid and dotted lines depict paths for adsorbate flow that are active and inactive respectively. As shown, discharging mode takes adsorbate from the reservoir, passes it through the evaporator

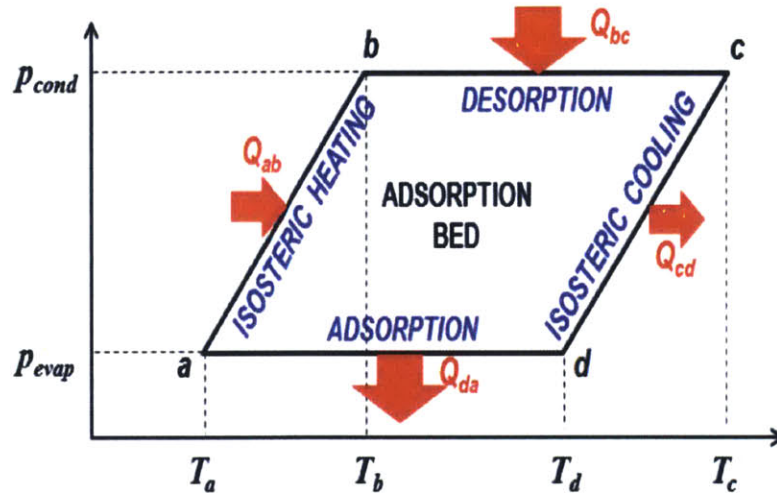


Figure 1: Pressure vs. temperature at the adsorption bed for an ATB operation cycle. Discharging mode, which generates heating and cooling energies, consists of isosteric cooling and adsorption, while recharging mode consumes energy through isosteric heating and desorption. Image published previously in [3].

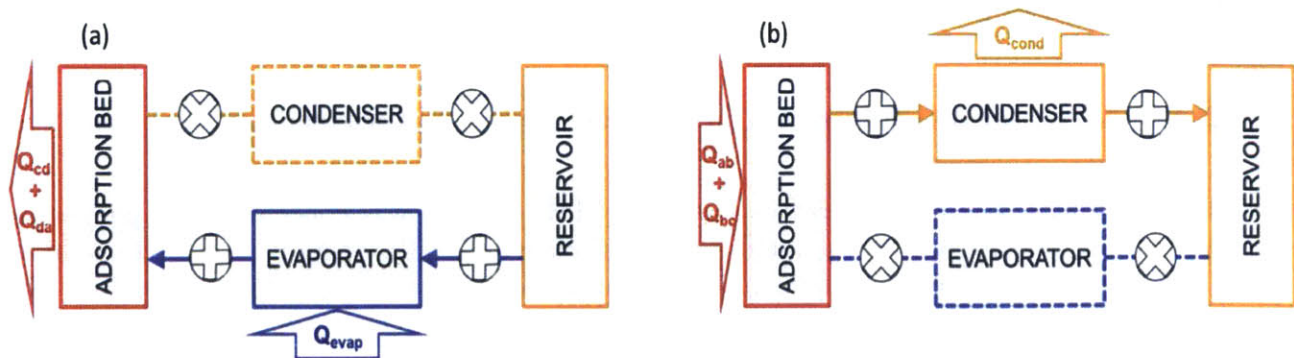


Figure 2: Schematic showing the operation of the ATB in its discharging mode (a) and recharging mode (b). Image published previously in [3].

where it consumes heat energy Q_{evap} to evaporate. This energy consumption can be used as a source of cooling. The vapor then flows into the adsorption bed where it is adsorbed, releasing heat of adsorption (Q_{da}) to the environment which can be used as a heating source. Q_{cd} is the heat released by the bed while it is cooled to the proper starting temperature before adsorption begins (process c-d).

Recharging mode (Fig. 2(b)) begins by inputting heat Q_{ab} into the adsorption bed, increasing the temperature of the bed and causing some of adsorbate to desorb. When the pressure reaches the saturation pressure corresponding to the condenser temperature (p_{cond}) the vapor begins to condense in the condenser, releasing Q_{cond} , and continues to do so while the bed temperature is raised to T_c . This condensed adsorbate returns to the reservoir, and the condenser valves are closed in preparation for the cooling process c-d that begins the next cycle.

In the ATB discussed in [3] the heat of adsorption can be used to heat the EV cabin during cold winter months and heat of evaporation can be extracted from the cabin to cool it during the summer. Recharging is performed on the grid, simultaneous to the charging of the car's electric battery.

2.2 Adsorbents

ATB operation is made possible by the properties of the adsorbent materials that are used to form the adsorption bed. Adsorbents are a class of micro-porous solids that allow an adsorbate in vapor form (such as water vapor) to bind to various sites in their micro-structures, releasing energy known as heat of adsorption. This binding process, known as adsorption, can occur as chemisorption, where a covalent bond is formed between adsorbent and adsorbed vapor, or as physisorption, where van der Waals and electrostatic interactions are the source of binding energy. This work focuses on the use MgY zeolite, a physisorbent, and thus going forward only physisorption will be considered. While no chemical bond is formed, the charged characteristics of certain adsorbates combined with the unique geometries and

ionic properties of these adsorbents enable heats of adsorption as high as 1.8 times the heat of vaporization (h_{fg}) of the adsorbate (in the case of water) [5].

Figure 3 shows the structure of an aluminosilicate zeolite [6]. The sodalite cages and supercage are prime locations for adsorption to occur and lead to the high uptake capacities (up to ~ 40 weight percent of water) of zeolites. Similar geometric structures serve the same purpose in other types of adsorbents.

Characterization of adsorbent properties is crucial to understanding how the material will behave in a system. Heat of adsorption and uptake capacity collectively characterize the total energy that can be generated from an amount of adsorbent for a given adsorbate. Heat of adsorption is a measure of the energy released by the process per mass of adsorbate, in units of [J/kg]. Uptake capacity (measured in weight percentage [wt%]) is the ratio of the mass of adsorbate that can be adsorbed per unit mass of adsorbent, and is characterized as a function of the relative pressure at a given temperature. Thus, if the mass of adsorbent is known it can be multiplied by the uptake capacity and then heat of adsorption to give the total energy that will be released by the adsorption process.

2.2.1 Adsorption Isotherms

The uptake capacity of an adsorbent-adsorbate pair is commonly plotted as a function of the relative pressure of the adsorbate at a fixed temperature. This type of plot is known as an adsorption isotherm (henceforth called just isotherm) [7]. The shape of an isotherm curve dictates the operating conditions of a system that uses adsorption to drive a process. The

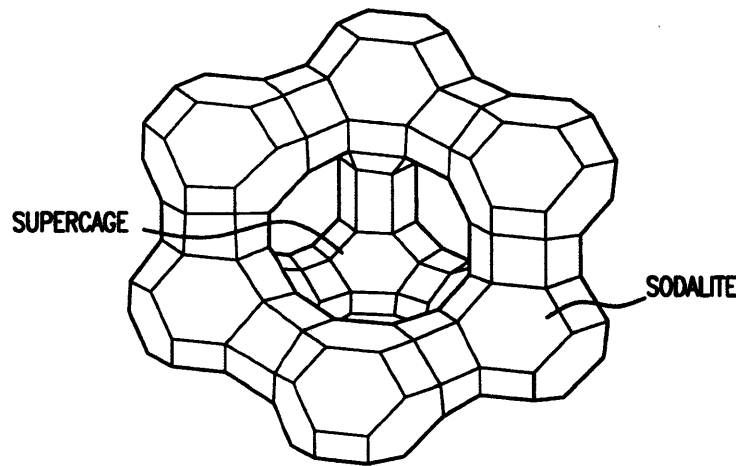


Figure 3: A representation of the geometry of an aluminosilicate zeolite. The supercage and sodalite cages are void spaces in the molecule that entrap adsorbate molecules and account for the high uptake of this adsorbent. Image adapted from Coq. et al. [6].

zeolite in this work has isotherms of Type I, which have a shape similar to that in Fig. 4 [2]. Type I adsorbents have high uptake capacities even at very low partial pressures (<5%) and thus can be operated under the saturation conditions of the adsorbate. As cooling power is generated by evaporation of the adsorbate, maintaining the adsorbate in a saturated state is ideal.

The useful quantity defined by the isotherm is the amount of adsorbate contained in an adsorbent sample of a known weight, which determines the amount that is adsorbed or desorbed by a process. As an example, a desorption process begins with a bed of adsorbent at a given relative pressure (RP) on an isotherm, say 0.2 RP on the isotherm in Figure 4. This indicates that water weighing about 27% of the dry adsorbent weight is held within the adsorption bed. The system conditions will then be controlled, via adjustment of adsorbent temperature, vapor temperature, or vapor pressure, such that the RP drops to a lower value, for example 0.02. Then the new amount of water that can be held in the bed is only about 21 wt%, meaning that 6 wt% of water was released from the bed. Of course, for an adsorption process the relative pressure begins at a low value and is brought to a higher value, allowing more vapor to adsorb in the adsorbent bed.

In both the adsorption and desorption processes, the adsorbent temperature may change since the rate of heat generation may not match that of dissipation, so the system conditions may correspond to a different isotherm. Also, since an isotherm is a steady state curve and the processes are transient, it is often difficult to tell the path along an isotherm or set of isotherms that is taken by a process. Instead, it is easier to simply look at the starting steady state condition, locate a point on an isotherm and find the uptake value and then do the same for the final condition and take the difference to determine the net change in uptake.

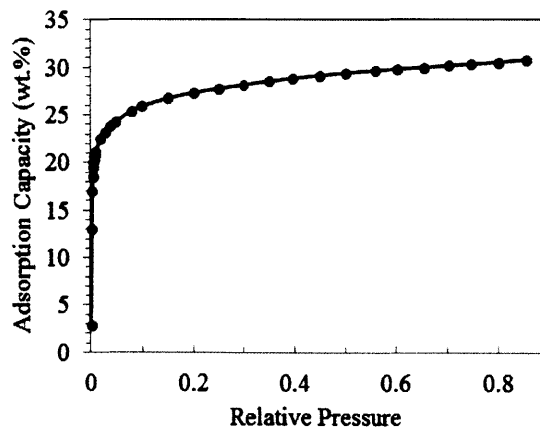


Figure 4: A representative Type I isotherm. This particular isotherm is plotted for Zeolite 13X (Sigma-Aldrich) with water adsorbate at 25°C. Image taken from [2].

2.2.2 Heat of Adsorption and Adsorption Energy

With the knowledge of change in uptake that can be determined from the adsorption isotherm and the starting and ending conditions of a process, the energy of the process can be determined. This energy can either be released as heat via the exothermic adsorption process or consumed by the endothermic desorption process. Either way, the energy is related to the change in uptake by the quantity known as the heat of adsorption of the adsorbent/adsorbate pair.

The heat of adsorption is analogous to the enthalpy of phase change of a material. On a molecular level, it is the amount of energy that is released when an adsorbate molecule binds to an adsorption site in the adsorbent's microstructure, or the energy that is required to break the bond. Adsorbents usually contain several different types of binding sites, with different bonding energies, and the bond strengths can also be affected by the amount of adsorbate occupying sites in the structure, so the heat of adsorption is not a constant quantity [8]. In general, the highest energy sites will bind adsorbate molecules first, due to their high affinity for the molecules, and then the adsorbate will fill the lower energy sites. Thus, the heat of adsorption is inversely proportional to the uptake, yet the functional relation is highly dependent on the adsorbent microstructure and the adsorbate molecular chemistry. It should be noted that this dependence holds in cases where the adsorbent-adsorbate interactions are stronger than adsorbate-adsorbate interactions (as is true for those exhibiting Type I isotherms) but may not be true in other cases.

Similar to how it is common to characterize the change in uptake by looking at steady state final and initial conditions, the heat of adsorption as a function of uptake or time is not of as much interest as the average over a process. In this work, since the total energy change of a process is of most importance, the heat of adsorption will be treated as a constant value equal to the average over the course of a process.

The total adsorption energy can be calculated by multiplying the mass of adsorbate involved in the adsorption process by the average heat of adsorption for that process. Of course, this is equivalent to integrating the heat of adsorption as a function of uptake over the total uptake and multiplying it by the mass of adsorbate. Therefore, the net energy for a process is given by Eq. 1:

$$E_{\text{ads}} = m_{\text{adsorbed}} h_{\text{ads}} = m_{\text{adsorbent}} \omega h_{\text{ads}} \quad (1)$$

where:

E_{ads} = adsorption energy [J]

m_{adsorbed} = mass of adsorbed adsorbate [kg]

$m_{\text{adsorbent}}$ = mass of the adsorbent sample [kg]

ω = uptake in weight percent (wt%) [kg adsorbate/kg adsorbent]

h_{ads} = heat of adsorption [J/kg adsorbate]

To give the heat of adsorption a familiar reference quantity, it is often written as the product of a constant, which we will call the heat of adsorption constant, and the heat of phase change of the adsorbate. In this work, the adsorbate is water, and the heat of adsorption typically lies between 1.5 and 1.8 times its heat of vaporization (h_{fg}) [9]. Cooling energy is produced by evaporation, which is calculated by the mass of water evaporated times the heat of vaporization. Since the evaporated water is essentially all adsorbed, the unitless heat of adsorption constant, k_{ads} , can be determined by the ratio of adsorption energy to evaporation energy. In equation form:

$$h_{ads} = k_{ads} h_{fg} \quad (2)$$

$$E_{evap} = m_{evap} h_{fg} \quad (3)$$

and since $m_{evap} = m_{adsorbed}$, combining the above equations with Eq. 1 gives

$$E_{ads} = m_{evap} k_{ads} h_{fg} = E_{evap} k_{ads} \quad (4)$$

which rearranges to

$$k_{ads} = \frac{E_{ads}}{E_{evap}} \quad (5)$$

2.3 Previous Small-Scale Prototype Work

Prior to the start of the work in this thesis, another Masters student had pioneered the effort to create a small-scale ATB to demonstrate that the ATB concept was feasible [4]. As discussed in his Masters thesis, Ian McKay built the ATB shown in Fig. 5, which contained about 200 grams of Zeolite 13X (a commercial Type I adsorbent).

This prototype included several novel design features. The integration of the evaporator and adsorption bed into a single enclosure is one of the most important, which reduces the vapor transport limitation between these two components. In this way, the evaporation energy can be used to cool the base of the enclosure and adsorption heating can heat the top. Figure 5 shows two finned-heat-exchangers (top and bottom of image) that facilitate the extraction of these energies and could be replaced by objects that require heating or cooling.

While this prototype was put through a series of experiments to characterize its operation, demonstrating the potential of the ATB concept, there were several design challenges

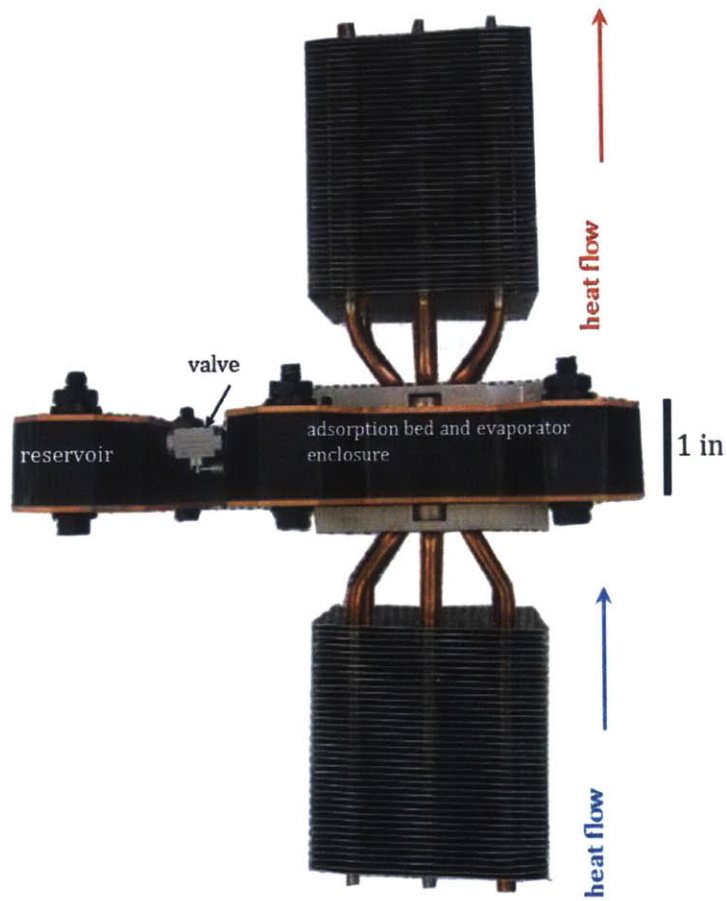


Figure 5: Image of the small-scale ATB prototype designed and fabricated by Ian McKay [4].

that prevented further work with this prototype. First, the sides of the enclosure that housed the adsorption bed and evaporator were made from ULTEM (ULTEM polyetherimide resin, Sabic Plastics). This material was found to contain micro-cracks in its structure, preventing the low internal pressures necessary for ATB operation. Thus, the prototype was only operational inside another larger vacuum chamber, restricting its operation to laboratory settings in which such a chamber is available. A second restriction was its size; while it was much smaller than a system that would be operated in an EV (which requires several kilograms of adsorbent material) it was too large for the novel adsorbent materials in development soon after its creation (such as MgY zeolite) which were only available on the tens of grams scale. These restrictions led to the conception of an even smaller ATB prototype, which began as the Button Cell Prototype and later evolved into the Dual Chamber Prototype.

2.4 Small-Scale ATB Prototype Objectives

2.4.1 Button Cell Prototype Objectives

Following the work of Ian McKay [4], who demonstrated the operation of many components of a small-scale Advanced Thermo-Adsorptive Battery (ATB) in a lab setting, it was desirable to build a complete prototype that could be operated outside the lab. Thus, the idea for the Button Cell Prototype was born, which would address the design challenges that had prevented integrated device operation.

The Button Cell Prototype was originally conceived to combine the work of Ian McKay into a device that could operate outside a vacuum chamber, yet the small form factor quickly opened the door for other project objectives. First, it could be used to show the potential of an ATB for commonplace heating and cooling applications. Contrary to the use of an ATB for climate control of a car, house, or similar applications requiring many kilograms of adsorbent and on the order of cubic meters in volume, the Button Cell could fit in the palm of a hand and be used for proportionally sized heating and cooling purposes. The ability to use the ATB technology for something as simple as heating oatmeal or cooling a beverage could spark interest in the technology while showing its diverse range of potential applications.

Additionally, the Button Cell Prototype volume was small enough that it could operate using novel, high performance adsorbents that were only available in small quantities. This would allow for system level testing of these new materials combined with novel binders that can enhance vapor and thermal transport within an adsorbent bed. As these adsorbents show higher material and component level performances than seen to date [10], the potential for the highest system level performance metric was also an objective.

The ability to show the highest energy and power densities from an adsorbent system of this sort led to a Button Cell Prototype design that aimed to minimize system volume and weight. A very compact design was developed, as will be discussed in Sect. 3.1.

2.4.2 Dual Chamber Prototype Objectives

The Dual Chamber Prototype was designed to eliminate the complications of the Button Cell Prototype and take over in pursuing its goals. Its design (as discussed in Sect. 4.1) also allows for better control over the conditions of the adsorbent bed and reservoir/evaporator/condenser, making several other goals possible. First, it is desirable to vary the temperature conditions of the adsorption bed and condenser during desorption to give an indication of how these conditions may be best optimized on a larger system. Similarly, varying the temperature conditions during adsorption can mimic the effects of changes in ambient temperature while using an ATB in an electric vehicle, predicting how the performance will change in different climates. Cyclability tests can also show how adsorbents will degrade over time, and the ability to observe cooling as well as heating will help determine if the degradation is to the

uptake capacity or heat of adsorption of the material. The ease of switching from one adsorbent bed sample to another in the prototype will allow these parameters to be explored for different adsorbents without affecting system operating conditions. Thus, direct comparisons can be made between adsorption beds that vary in adsorbent type, binder type, density, and/or volume.

While the Button Cell Prototype was ideally going to be a demonstration of a product created with this technology, the Dual Chamber Prototype aims to be a platform for testing the ATB as a system. The Dual Chamber Prototype is therefore not optimized for maximum power or energy densities but is instead arranged such that experimental conditions are easily controllable. This enables parameter variations to demonstrate various operating conditions and quantitatively predict how ATB systems will behave.

2.5 Small-Scale ATB Concepts

2.5.1 Button Cell Prototype

A simple description of the Button Cell Prototype system set-up is as follows, and is depicted in Fig. 6:

- A **Reservoir** holds the refrigerant in saturated liquid/vapor form
- A **Valve** (or multiple valves) separates this refrigerant from the rest of the system
- A porous **Evaporator Medium** blocks the refrigerant pathway to the adsorbent bed
- A **Vapor Gap** separates the Evaporator Medium from the **Adsorption Bed**, thermally isolating these two components
- All components are housed within a vacuum sealed enclosure

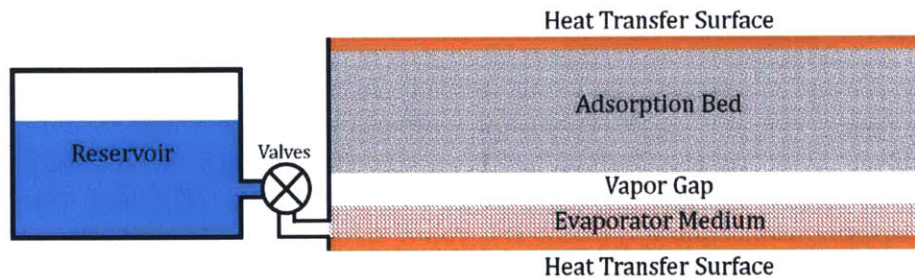


Figure 6: A schematic of the setup of the Button Cell Prototype.

In order for the system to operate, several conditions must be met. The enclosure must be completely leak free. The admission of any gas from the environment into the system will disrupt the controlled internal pressure and prevent proper operation. The valves separating reservoir from adsorption bed must be able to prevent all water vapor from crossing from one side to the other in the closed position, even with a large pressure difference as a driving

force. They must also allow liquid to flow through them in the open position. The evaporator medium needs to be permeable for water vapor without allowing liquid to pass through. This is crucial in the prevention of system flooding, which is a common failure mode. Last, the system must contain minimal air or gases other than the adsorbate vapor. Thus it must be properly evacuated prior to filling with adsorbate, and the adsorbate must be sufficiently degased.

The basic principle of Button Cell operation is to pass the adsorbate through the evaporator medium and into the adsorbent bed. In the system shown in Fig. 6, the refrigerant originates in the reservoir which is separated from the evaporator and adsorbent bed by a valve. When the valve is open, the difference in pressure between the inside of the reservoir (at $P_{\text{sat}}(T_{\text{reservoir}})$) and the vapor gap drives refrigerant transport. The pressure drop incurred during this transport through the evaporator medium causes evaporation, as the pressure drops below the saturation pressure at the given system temperature, which pulls heat from the lower heat transfer surface. The vapor that permeates through the evaporator travels across the vapor gap and is adsorbed in the bed, releasing the heat of adsorption to the upper heat transfer surface. The upper heat transfer surface can be interfaced with a system that requires heat input while the lower can be interfaced with one that requires heat rejection.

The required pressure drop for evaporation will ideally occur within the evaporator, yet if it does not then liquid may penetrate through the evaporator, entering the vapor gap and possibly coming into contact with the adsorption bed. This is known as evaporator flooding and is a major failure mode of the system. If flooding occurs, the performance decreases for two reasons. First, the evaporation that should occur in the evaporator instead occurs at the adsorbent bed surface, pulling energy from the bed for that process and detracting from the heat of adsorption. This degrades both heating and cooling performances. Second, the liquid inside the vapor gap can act as a thermal short, creating a thermal conduction path between the hot adsorption bed and the cold evaporator. Flooding prevention was a large area of study in the overall ATB work, and ultimately helped shape the decision to change the evaporator design.

During normal operation, the vapor pressure leaving the evaporator medium will range from $P_{\text{sat}}(T_{\text{amb}})$, where T_{amb} is the initial temperature of the whole system, to $P_{\text{sat}}(T_{\text{low}})$, once the lower heat transfer surface has been cooled substantially. A target value for T_{low} is 3°C which corresponds to a saturation pressure of 760 Pa. The high rate of adsorption for most of operation should sustain the vapor gap at a lower pressure, although as the adsorbent begins to saturate this pressure will increase and eventually equilibrate with the vapor pressure at the evaporator surface. The reservoir, which should be reasonably thermally insulated from the evaporator, will maintain a temperature of T_{amb} and hold 2-phase adsorbate at the corresponding saturation pressure.

Going into a bit more detail, Fig. 7 shows system operation as time progresses from (a) to (e) under reasonable ambient conditions. Part (a) shows the beginning state where the adsorption bed is free of vapor and the reservoir is closed. All components are at an initial temperature of 25°C, the refrigerant is at the saturation pressure corresponding to

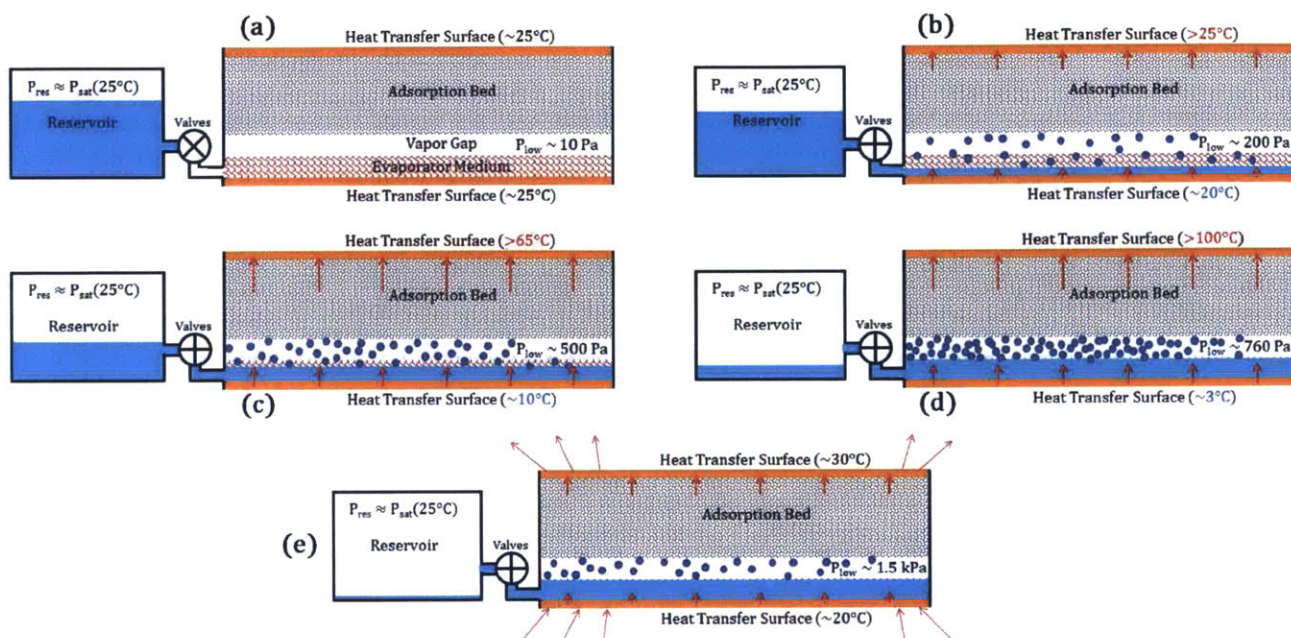


Figure 7: A representation of the heating/cooling mode of operation of the Button Cell Prototype, progressing from (a) to (e) (see text).

this temperature and the vapor gap is at the low pressure of $\sim 10\text{ Pa}$. In (b) the valve is opened and the pressure difference from the reservoir to the vapor gap drives flow of liquid through the evaporator medium. Flow-induced pressure drop causes evaporation and cools the lower surface, releasing vapor which is in turn adsorbed by the adsorbent, heating the upper surface. As the lower surface cools, the lower temperature in the reservoir requires a larger pressure drop for evaporation and so liquid penetrates farther into the evaporator, as shown in (c). In (d), the entirety of the reservoir is utilized, corresponding to the point of maximum performance where the lower heat transfer surface is at $\sim 3^\circ\text{C}$ and the upper is in excess of 100°C . After this point is reached the process begins to slow and the system begins to return to an inactive (saturated) state, as shown in (e).

In order for this process to be repeated, the system must be ‘recharged’ to remove the refrigerant from the adsorbent and return it to the reservoir, which is known as the desorption process. This can be accomplished by opening the valve and applying heat to the upper heat transfer surface while keeping the reservoir cool. The heated adsorbent desorbs to the extent it can with the heat energy provided, releasing vapor back into the vapor gap at a saturation pressure corresponding to the temperature. The lower temperature of the reservoir leads to a lower saturation pressure, encouraging the vapor to return and condense on the reservoir walls. A source of cooling is necessary to remove all sensible heat from the vapor and provide energy for phase change.

2.5.2 Dual Chamber Prototype

The Dual Chamber Prototype configuration, depicted in Fig. 8, is essentially an expanded version of the Button Cell configuration, where the evaporator/condenser is moved away from the adsorbent bed. It consists of two distinct chambers (hence the name) separated by tubing and a pair of valves. The two valves may appear redundant, and as shown in the figure one valve is all that is necessary, but more connections are added to the system during testing, giving both valves distinct purpose. This will be discussed in detail in Sect. 4.2.

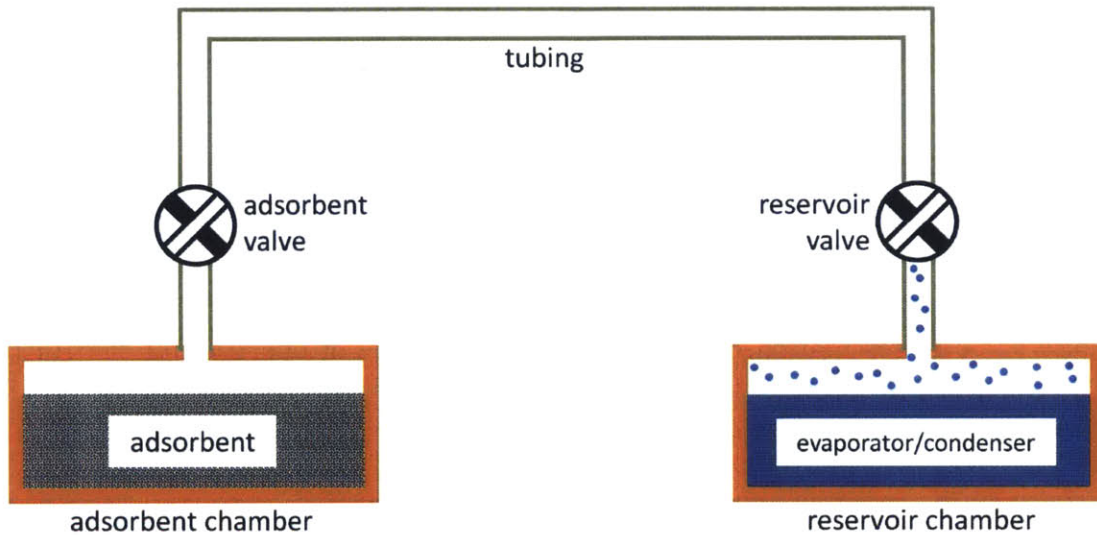


Figure 8: Schematic of the Dual Chamber Prototype. Two chambers house the adsorbent and evaporator/condenser, and are interfaced with one another via tubing. Two valves allow separation of the chambers from one another.

The chamber on the left contains the adsorption bed and the one on the right contains the evaporator/condenser and also serves as the reservoir. The tubing enables flow of vapor from one chamber to the other, which allows the adsorption and desorption processes to occur. An upside-down U shape was selected for this system for two reasons. The first was to allow both chambers a bottom surface that could be used to transfer heat out of the system, which can be measured and monitored using thin-film heat-flux sensors. The second is that the shape of the tubing discourages the passage of liquid from one chamber to the other by adding a height barrier, since only vapor should flow in the system.

The Dual Chamber Prototype generates heating and cooling power in a very similar way to the Button Cell Prototype, yet the adsorbent bed is kept in a different chamber from the evaporator/condenser which is now placed inside the reservoir. The essential mode of operation, in which usable heating/cooling energies are produced, is adsorption, and a schematic of this can be seen in Fig. 9.

Beginning with Fig. 9 part (a), the Dual Chamber system is in thermal equilibrium with the ambient. Both the valves are closed, keeping the adsorbent bed and tubing devoid of

liquid, at an extremely low pressure. The reservoir begins with the evaporator/condenser (metal foam) filled with saturated liquid and the remaining volume filled with saturated vapor. Fig. 9(b) shows the start of the adsorption process, which begins by opening the valves, creating a pathway between the two chambers. The saturated vapor in the reservoir quickly expands to fill this extra volume, decreasing the pressure in the reservoir. Next, as depicted in (c), liquid in the reservoir evaporates to maintain the saturation pressure, cooling the evaporator/condenser and reservoir chamber. Vapor that reaches the adsorbent is adsorbed, releasing heat to the adsorbent chamber. The cold reservoir chamber is used to provide cooling from its base and the heated adsorbent chamber provides heating from its base. Next, as in (d), the process continues, with the adsorbent removing vapor from the tubes, creating a low pressure environment. The low pressure drives evaporation of the liquid inside the reservoir. As the process continues, pressures in the system begin to increase, increasing the rates of adsorption and evaporation. The temperature in the reservoir continues to drop and that in the adsorbent bed rises. The differences in these temperatures from ambient will reach maximal values, corresponding to the instant of maximum power of the system.

Continuing on to Fig. 9(e), the bed is beginning to saturate, decreasing the rates of adsorption and evaporation. The pressure everywhere inside the system increases, since the

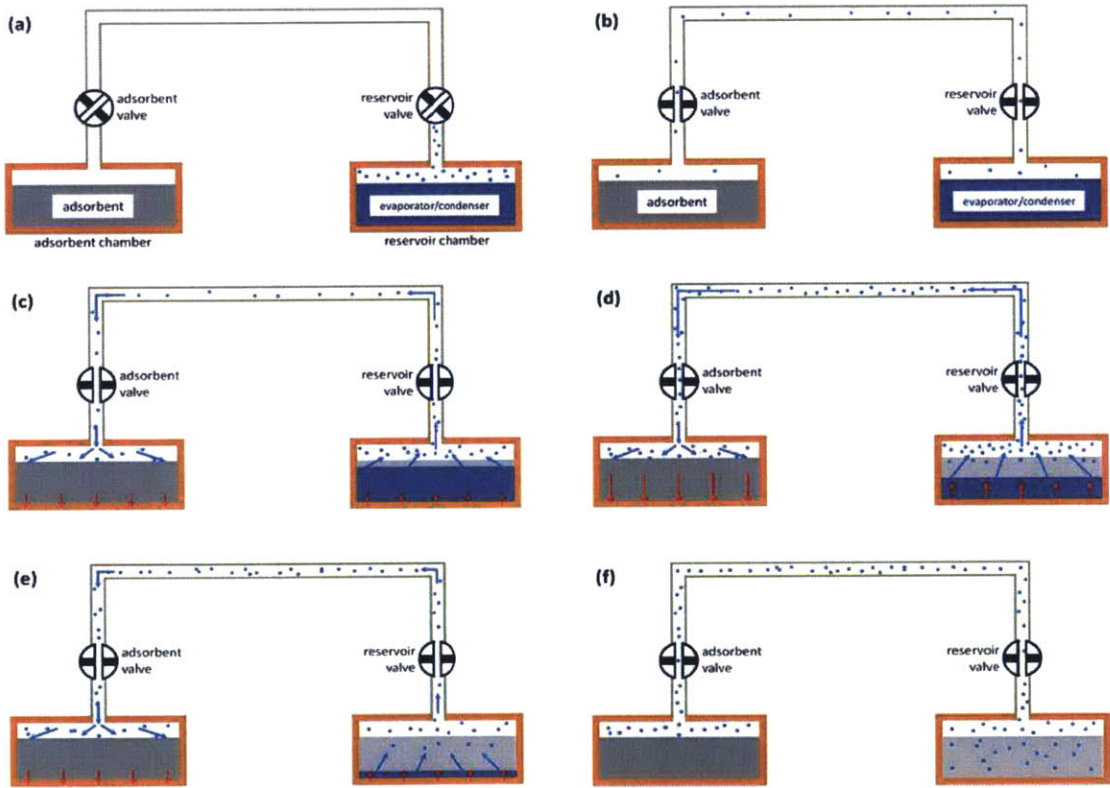


Figure 9: The above figure shows a schematic of the adsorption process of the Dual Chamber Prototype, progressing from (a) to (f) (see text).

adsorbent cannot remove vapor as fast as it can be generated by evaporation, approaching the saturation pressure corresponding to the reservoir temperature. Finally, as shown in Fig. 9(f), the adsorption bed becomes fully saturated, so the driving force for vapor transport is no longer present. The reservoir at this point is approximately empty, and some amount of remaining water fills the system as saturated vapor. All system components return to the ambient temperature, and the system reaches a final steady state equilibrium.

The recharging process, desorption/condensation mode, takes an energy input and uses it to remove vapor from the adsorbent bed and place it back in the reservoir as liquid. Figure 10 depicts this mode in schematic form. The starting condition is generally the same as the ending condition of desorption, depicted in Fig. 9(f), which is shown again in Fig. 10(a), with the only difference being the closed reservoir valve.

The beginning of the desorption process is illustrated in Fig. 10(b), where external heat sources are used to heat the adsorbent chamber and all of the system tubing, causing desorption and increasing the internal vapor pressure. Another external source (usually a chiller) can be used to keep the base of the reservoir chamber at a constant low temperature. This constant low temperature provides the energy for condensation required inside the reservoir. Then, proceeding to Fig. 10(c), the condensation process begins by opening the reservoir

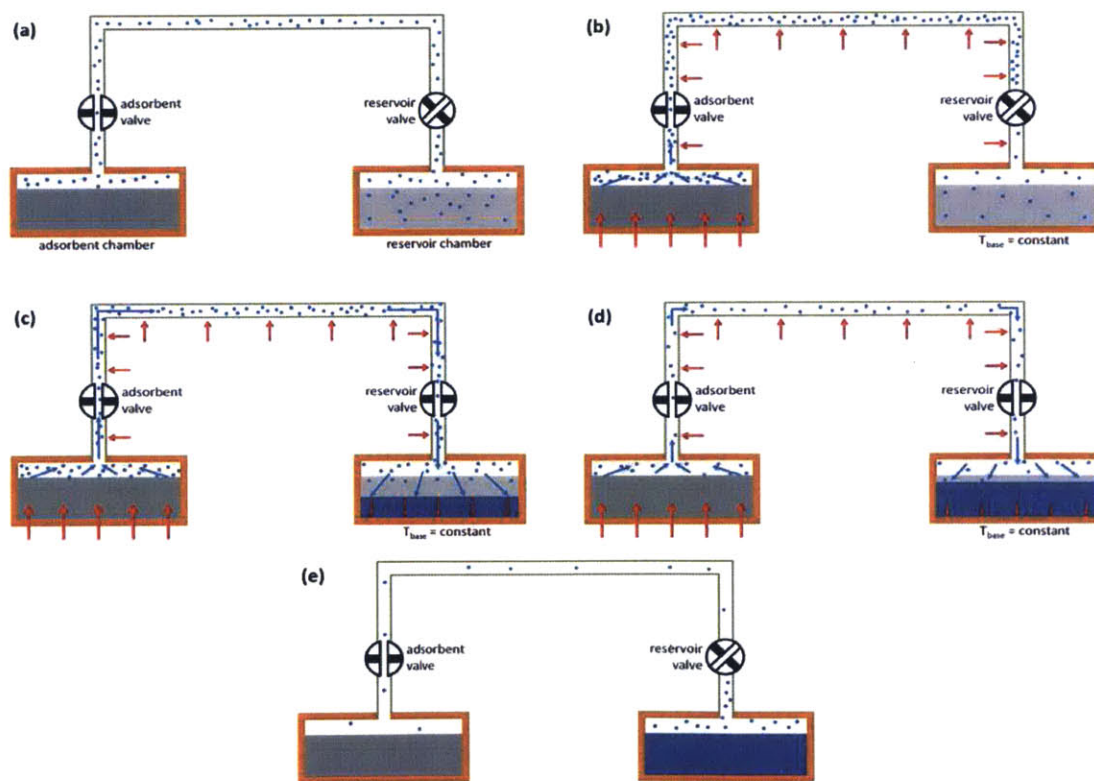


Figure 10: A schematic of the desorption process of the Dual Chamber Prototype, progressing from (a) to (e) (see text).

valve. This causes a flow of high pressure vapor (that was desorbed from the adsorbent and heated in the adsorbent chamber and tubing) into the reservoir. Since the evaporator/condenser is in close thermal contact with the cooled reservoir base, the vapor condenses and collects inside the reservoir, releasing the heat of phase change to the reservoir chamber. This enthalpy of condensation can be measured as a function of time using a heat-flux sensor below the reservoir base, and can be used to calculate the amount of liquid that condensed. This can also be used to estimate the amount of desorbed vapor by conservation of mass.

Moving on to Fig. 10 part (d), the rate of desorption decreases since much of the vapor has already been removed from the adsorbent. Thus, the rate of vapor transport slows, which in turn slows the condensation rate. The reservoir still fills with liquid, yet at a slower rate, and a smaller amount of heat is released by the condensation process. The adsorbent chamber and tubes are still heated and kept at high temperatures to drive vapor into the reservoir and to reduce the possibility of condensing elsewhere in the system. Figure 10(e) shows the final configuration of the desorption/condensation process. Once the heat flux below the reservoir base approaches its steady state value (the same value as before condensation began) the condensation process is complete, and the reservoir valve is closed. While it is possible that the adsorbent is not fully desorbed, the end of condensation indicates the completion of desorption for the set operation conditions. The heaters and chiller are turned off, and the whole system is allowed to return to ambient temperature. The adsorbent will re-adsorb some of the vapor remaining in the tubing, which from an energy standpoint is an almost negligible quantity since the density of vapor is on the order of 1000 times lower than that of liquid [11], leaving the tubing at a pressure lower than the saturation pressure at ambient temperature.

3 Button Cell Prototype

3.1 Button Cell Prototype Design

The Button Cell Prototype design went through numerous iterations, landing on the configuration in Fig. 11, which is shown in an exploded view in Fig. 12. The design reflects the schematics shown in Figs. 6 and 7, with the reservoir on the left hand side, valves in the middle, and evaporator and adsorbent bed housed in an enclosure on the right. Note that the Button Cell Prototype size is significantly smaller than the previous small-scale prototype (shown in Fig. 5). The adsorption bed and evaporator enclosure has an internal volume of $\sim 16 \text{ cm}^3$ and is designed to hold around half that volume in adsorbent material. The adsorbent density is usually around 0.5 g/cm^3 in the foam binders used in the prototype, meaning around 4 g of adsorbent will be used. Thus the Button Cell Prototype is about 1/50th the scale of the previous prototype by adsorbent volume, enabling the use of novel materials that were only available on this scale.

The design also aimed to eliminate the issues that prevented low internal pressures in the first small-scale prototype, specifically the use of ULTEM and rubber gaskets in the structure. Instead, the entire Button Cell Prototype was designed using metal components with solder to bind them together. The bulk of the reservoir was milled from a block of brass (Ultra-Machinable 360 Brass, McMaster-Carr), chosen for its machinability and wettability to lead-tin-silver solder. The reservoir lid and tube are copper (Multipurpose 110 copper, McMaster-Carr) and are soldered to the top. The reservoir tube allows the whole system to be evacuated using a vacuum pump and filled with degassed liquid, which is the basis for

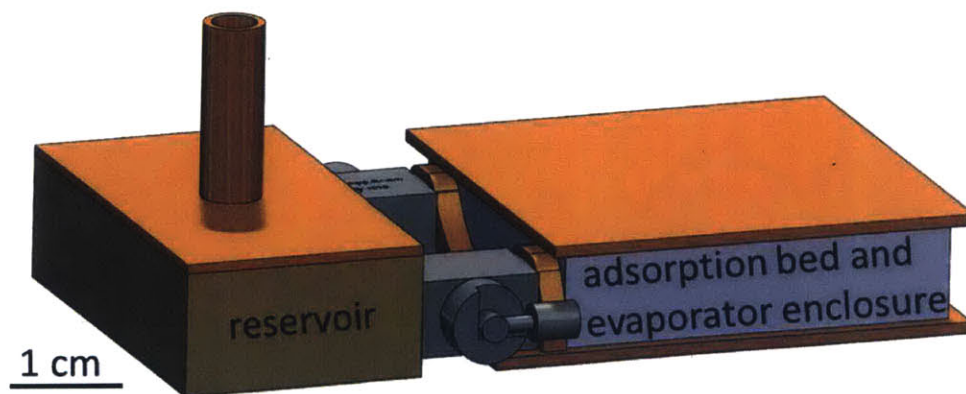


Figure 11: CAD model of the final Button Cell Prototype design. On the left, the reservoir consists of a hollow brass base with a bonded copper top and a tube attached for filling. In the center, two valves serve to interface the reservoir to the steel shell which forms the side walls of the chamber on the right. Inside this steel shell are the evaporator medium, bonded to the bottom surface, and adsorbent bed which is bonded to the top. These components can be seen in Fig. 12.

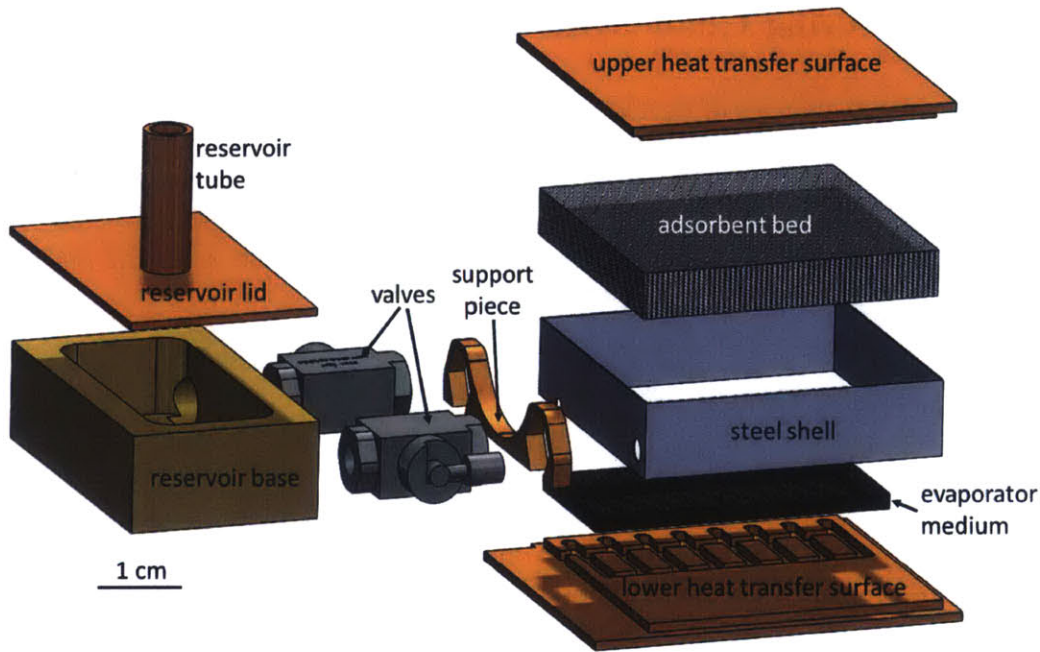


Figure 12: Exploded CAD model of the Button Cell Prototype design.

the preconditioning process.

The valves (Beswick MBV-1010) are ball valves made primarily of steel with an internal Teflon seal. These valves were chosen for their compactness and vacuum-compatibility, as well as the fact that their steel construction would not thermally conduct from the reservoir to the evaporator as much as alternative materials, such as brass. The copper support piece was added late in the design process to serve as a wetting interface for solder to help bond the valves to the steel shell, which proved to be one of the greatest challenges in the prototype construction.

As described in Section 2.5.1, the key to harnessing useful energy from the Button Cell Prototype system is the ability to create a large temperature difference between the upper and lower heat transfer surfaces. The hot upper surface can be used to heat an object while the lower surface can cool another. Thus, it was necessary to make those two surfaces thermally conducting while keeping them insulated from one another. To accomplish this, the heat transfer surfaces were machined from copper, and the interface between them is a very thin (0.0015" thick) steel shell which can hold vacuum while minimizing conduction and fin convection losses. This shell was shown to have a comparable thermal resistance to the ULTEM used in [4], so similar thermal short characteristics were assumed.

3.2 Manufacturing Challenges

Among the biggest challenges of developing the Button Cell Prototype was vacuum sealing. The device must have an internal volume that is free of air, allowing the internal pressures to be governed by the evaporation and adsorption processes. These pressures are on the order of several kilo-Pascals at most, so the enclosure must be able to withstand the large atmospheric pressure acting on the outside without springing leaks over the entire device lifetime. As such, an incredibly robust method for sealing was required.

3.2.1 Design Restrictions

It may appear trivial to form such a seal, as there are probably thousands of products available that are sealed to this extent, yet the design of the button cell provides unique complications. The first is the necessity for different metals to form different parts of the system. The close proximity of the generation of heating and cooling requires a good insulator to prevent thermal short losses. Very thin steel can serve this purpose. In contrast, the heating and cooling powers must be conducted away from their sources with low thermal resistance, making copper the ideal material to interface with the adsorbent and evaporator. A leak-tight joint must be made between these copper and steel components, and bonding dissimilar metals is always a challenging process. Similarly, the steel ball valves must be attached to the brass reservoir in addition to the previously mentioned copper and steel components.

The second complication is the temperature restrictions on the components during the bonding processes. The valves have internal seals made of Teflon, limiting the temperature to around 200°C. Also, the thin steel insulating shell (~0.0015 in. thick) tended to warp when heated with a torch, making brazing of this component to copper impractical. This leaves only low-temperature soldering as a viable bonding option, making it all the more tricky to attach the steel components, which have a tendency to not wet to solder.

3.2.2 Bonding Differing Materials

A possible solution to these problems came in the form of two electro-plating processes to coat the surfaces of steel with nickel and then copper, enabling all components to be joined together using lead-tin-silver (Pb36 Sn62 Ag2) solder at temperatures below 200°C. Figure 13 shows the process on one of the steel ball valves. The steel component is first electroplated with nickel in step 1. The nickel coating allows the steel to be plated with copper, as shown in step 2, the product of which is shown in the third image in the figure. Finally, using flux and a solder bath, the component can be tinned to guarantee full wetting from solder as shown in step 3, which allows for bonding to other system components.

An additional concern was the multiple solder joints bonding the system together. Originally, the plan was to bond the prototype together at several different temperatures, so first

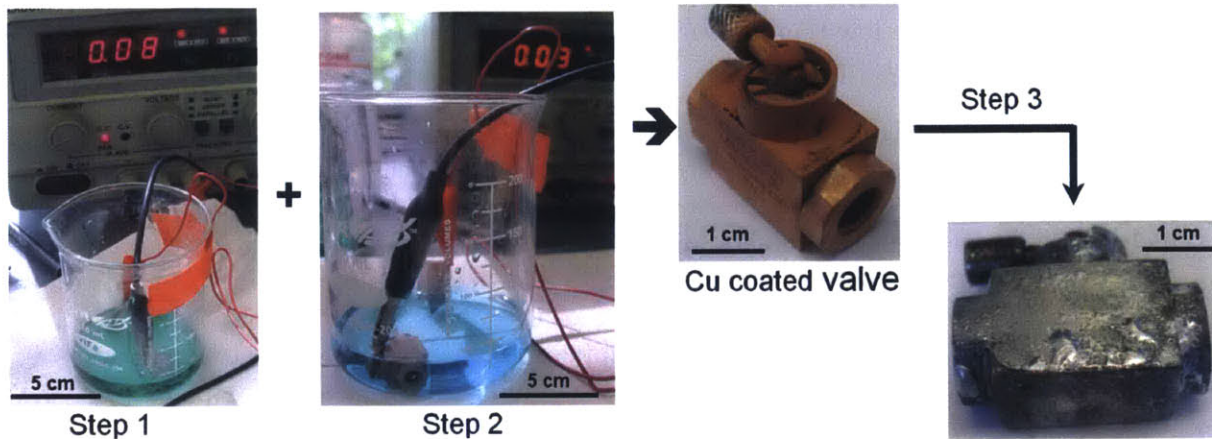


Figure 13: Images of the electroplating process that enables soldering of the steel components in the Button Cell Prototype. In step 1, the steel is electroplated with a layer of nickel, which allows it to be coated next with copper (step 2). The product of these two steps is the copper colored component, which can then be tinned with solder using flux and a high temperature solder bath.

some components could be bonded with a high-temperature braze which would stay bonded while others were joined at a lower temperature and so on. However, the temperature limitations of the valves and steel shell discouraged this process, so instead all components were

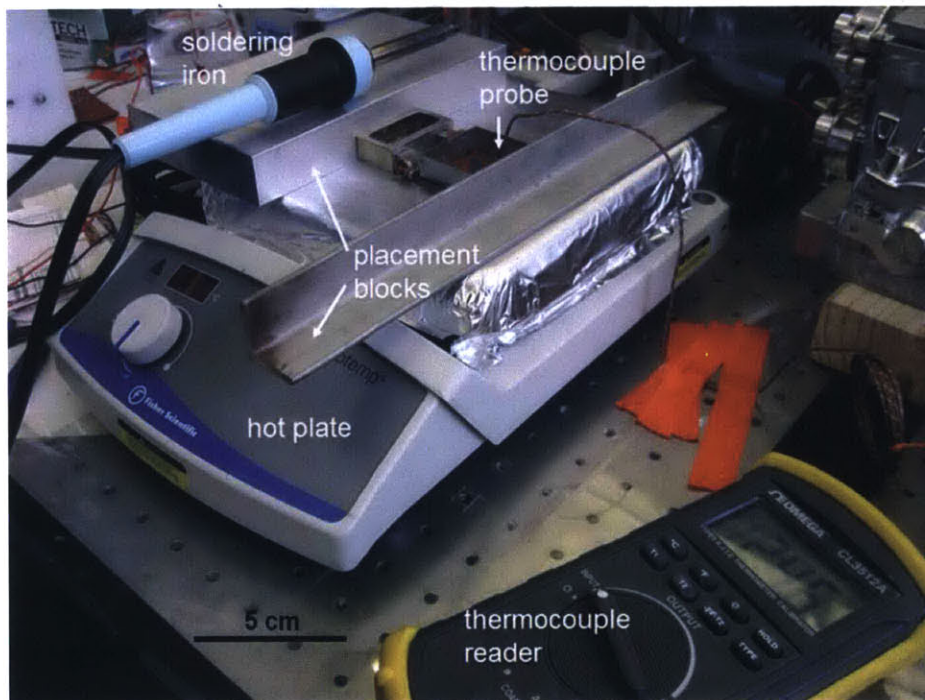


Figure 14: Photo of the soldering setup.

joined using the same low-temperature solder. As such, the soldering of all components was performed at the same time.

To enable soldering of multiple components at the same time, the setup shown in Fig. 14 was used. The components were arranged in their proper locations with respect to one another on the surface of a hot plate which was heated to around 175°C, slightly below the melting temperature of the solder. Metal placement blocks were placed on the hot plate to prevent the components from moving. A hand-held thermocouple reader was used to locally probe the system to verify the temperature of the various components. Then a soldering iron, at higher than the solder melting temperature, was used to locally heat areas to be soldered while applying solder and flux. Combining the iron and hot plate proved very useful in addressing leaks, since the leak location could be re-soldered without melting the surrounding solder joints.

The Button Cell Prototype design facilitated the soldering process in that the components were all aligned from the same orientation, and could be held on by gravity. In other words, the bottom layer of components was soldered together, then components were placed above those and soldered on, and then above those. This process allowed for the creation of

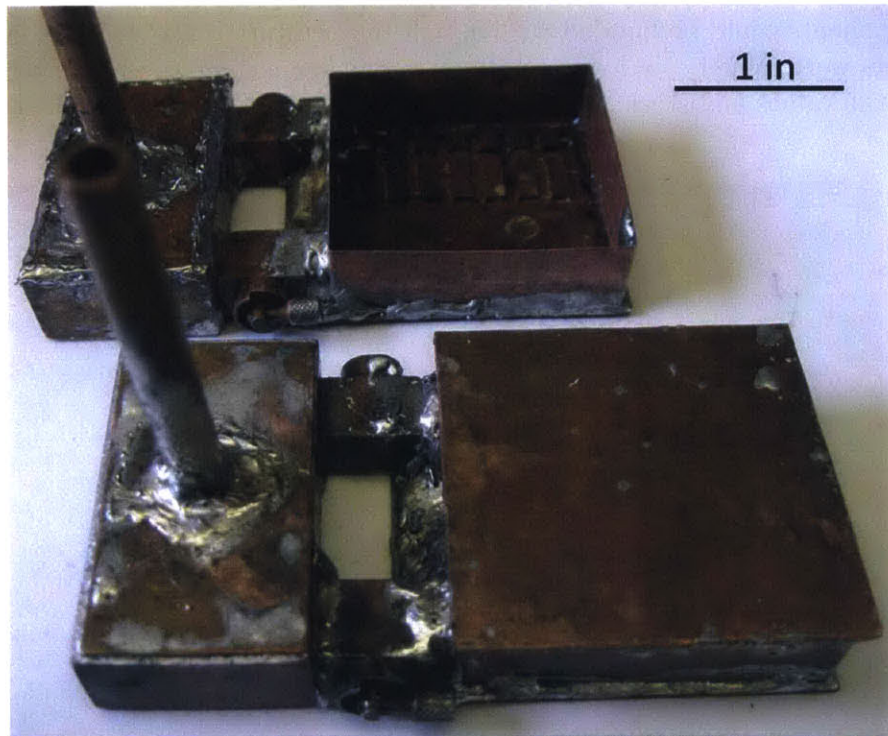


Figure 15: Image of the two Button Cell Prototypes that were made using the final design and fully soldered joints. The prototype in back of the image has the lid to the adsorbent side removed and does not contain the evaporator or adsorbent elements. Those elements were bonded using high thermal conductivity epoxy, and the lid was soldered on later by placing the whole system back on the soldering setup.

the two button cell prototypes in Figure 15 (the prototype in back has the lid removed and is void of evaporator and adsorbent components in this picture). Ultimately, despite many construction iterations and design modifications, it was too difficult to form the necessary vacuum seal using the above methods and the prototype design was put to rest. The construction methodology was put to use in the next prototype, where the same soldering setup was used to successfully bond and seal the chambers of the Dual Chamber Prototype.

4 Dual Chamber Prototype

4.1 Dual Chamber Prototype Design

As discussed in Section 2.4.2, the Dual Chamber Prototype had several of the design restrictions that plagued the Button Cell lifted, enabling a much simpler design. The decision was made to use the reservoir to house a metal foam which serves both as an evaporator and condenser. This allowed (and in fact necessitated) a larger distance between the evaporator and adsorption bed. Additionally, the idea that the small scale system will no longer be a demonstration of a potential product but instead a testing system enabled the use of off the shelf vacuum components, including valves and T junctions, which would have contributed too much thermal mass otherwise.

A CAD picture of the final Dual Chamber Prototype design is shown in Fig. 16, and a photo of the setup in the lab can be seen in Fig. 17. In this photo, taken from behind the setup, the reservoir chamber is on the left and the adsorbent chamber is on the right. As visible in the photo, this prototype was designed primarily using copper and brass to prevent the dissimilar metal complications discussed in Sect. 3.2.2. Inside the adsorbent chamber is a sample made from an adsorbent infiltrated into a porous nickel foam for structural and

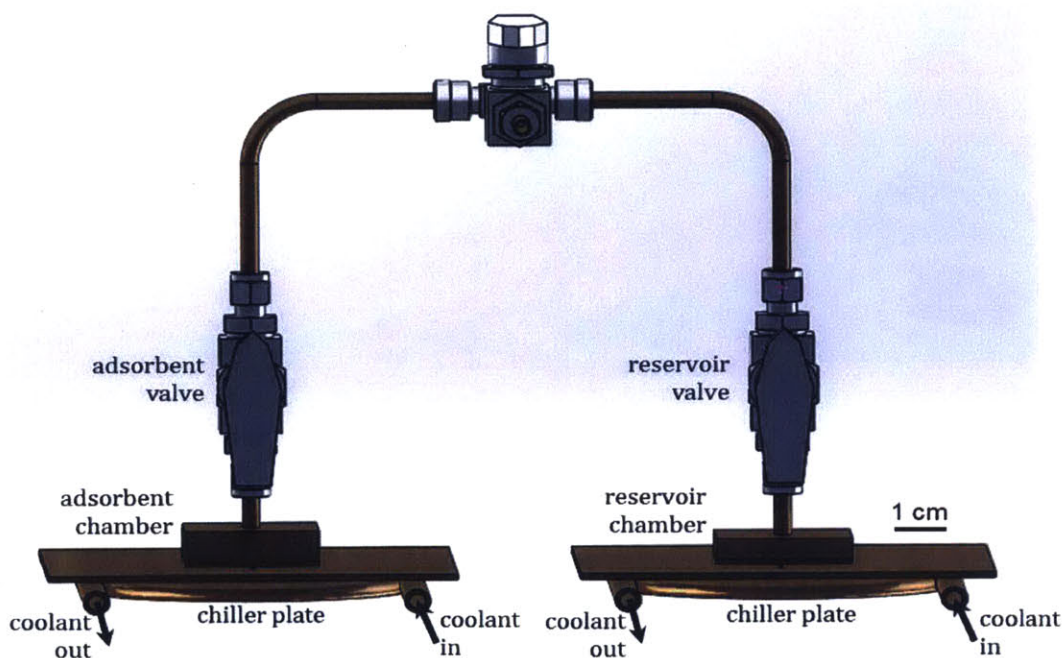


Figure 16: CAD image of the Dual Chamber Prototype design. It consists of two separate chambers, one housing the adsorbent bed (on the left) and one serving as the reservoir (right). These are interfaced with one another with quarter inch tubing and vacuum compatible valves, and sit atop chiller plates that allow for a controlled temperature.

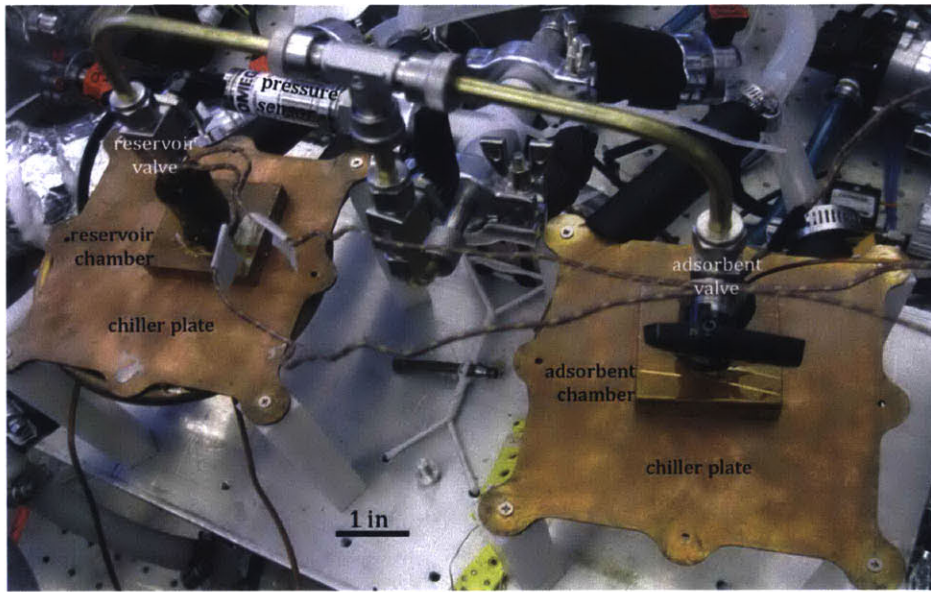


Figure 17: Picture of the Dual Chamber Prototype set up in the lab.

thermal binding (Fig. 18, left). The reservoir chamber contains a plain nickel foam soldered to its base to enhance heat transfer during evaporation and condensation (Fig. 18, right). While copper foam would be a better choice, due to its higher thermal conductivity, it was not available in the correct thickness ($\sim 6\text{mm}$).

Unlike the Button Cell Prototype, this new design separates the adsorbent from the reservoir (which also serves as evaporator and condenser) by quarter-inch tubing in an upside-down U-shape. This reduces the risk of thermal shorting during operation, enables the use of off-the-shelf valves and allows both chambers to be made entirely of copper. The chambers were machined from copper blocks and sealed to a copper base plate and brass tube using lead-tin-silver (Pb62 Sn36 Ag2) solder. Figure 19 part (a) shows these components before

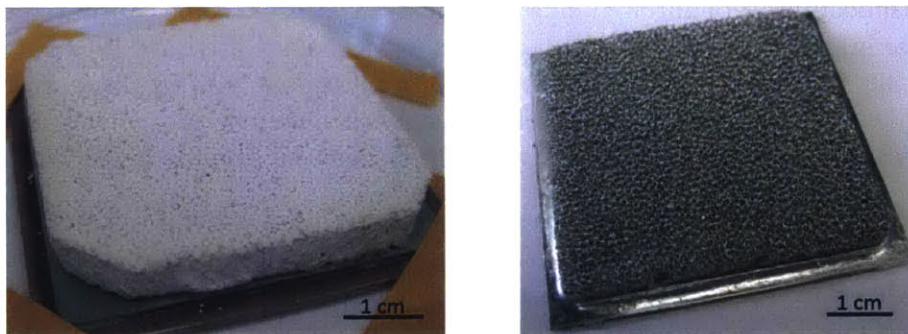


Figure 18: Pictures of the MgY Zeolite sample that is housed inside the adsorbent chamber (left) and the plain nickel foam that is inside the reservoir to enhance heat transfer for evaporation and condensation (right).

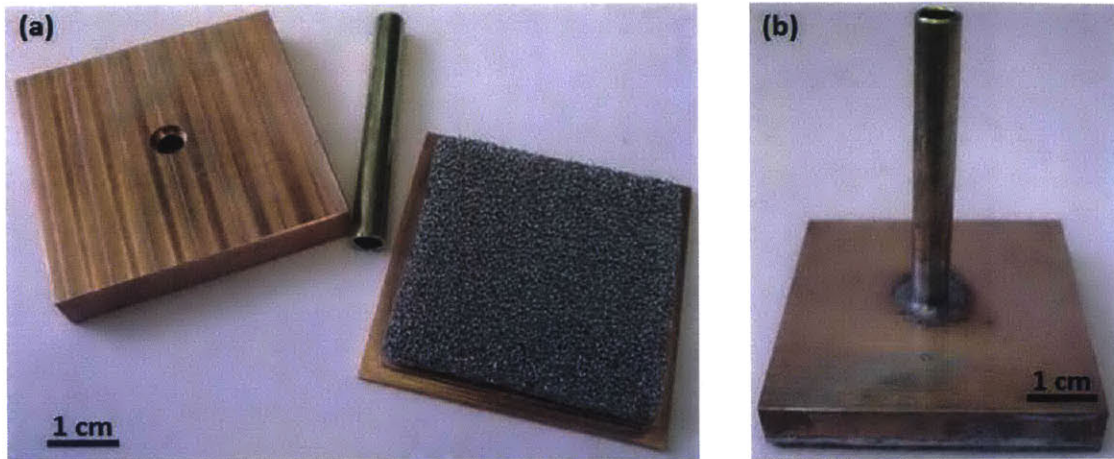


Figure 19: Figure (a) shows the 3 components that are soldered together to make (in this case) the reservoir chamber. The nickel foam pictured on the base plate is soldered to that plate inside the reservoir to provide extra surface area for evaporation and condensation to help enhance the heat transfer to the base. The adsorbent side looks much the same but uses a nickel foam that is infiltrated with adsorbent. Figure (b) shows the components soldered together. The foam sits on the inside, with about 2mm of space above it.

soldering, and part (b) shows them bonded together.

As can be seen in Figs. 16 and 17, vacuum compatible valves (Swagelok SS-42GS4) are placed directly above each chamber to allow isolation from the rest of the system, and another valve is attached with a T-junction at the top of the U. This valve connects to another T that connects to a pressure sensor (Omega PX409-005A5V) and then to a vacuum pump (Edwards RV3) via a liquid nitrogen trap. A schematic of the system setup is shown in Fig. 20. Valves A through D enable various modes of operation, including leak testing, desorption, and adsorption, which are monitored using the pressure sensor (denoted as P), the two heat-flux sensors (Omega HFS-3 and/or HFS-4) denoted HFS1 and HFS2, and the seven thermocouples (T1 through T7). The heat-flux sensors come calibrated by Omega and have a maximum error of $\pm 10\%$ [12]. The thermocouples used are K-type, with errors of $\pm 2.2^\circ\text{C}$ [13]. These sensors are monitored using an Agilent 34972A data acquisition system (DAQ). The vacuum pump in the schematic is also switched for a helium leak detector (Adixen ASM 142) during fabrication to identify and seal small leaks in the setup.

The upside-down U-shape geometry was chosen so that the base of each chamber can sit easily on top of a chiller plate to keep a controlled temperature below. Between the base of each chamber and chiller plate is a heat flux sensor to measure the heat fluxes during system operation (Omega HFS-3 is attached beneath the reservoir chamber and Omega HFS-4 is beneath the adsorbent chamber). Since the heat flux sensors are smaller than the chamber bases, they were mounted to each base using a double-sided Kapton[®] tape and surrounded by several layers of single-sided Kapton[®] tape, making the entire surface smooth and flat (see Fig. 21). The sensors are made primarily of Kapton[®] and thus have the same thermal

conductivity as the tape, allowing for a uniform heat flux to flow through the entire base of each chamber and into the chiller plate below.

While this heat flux sensor mounting configuration was used for a number of experiments,

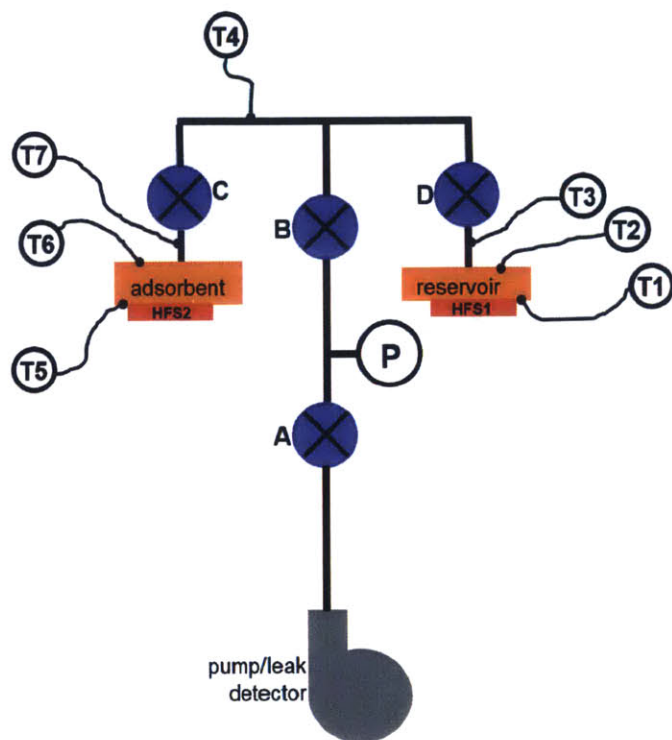


Figure 20: Schematic of the Dual Chamber Prototype setup.

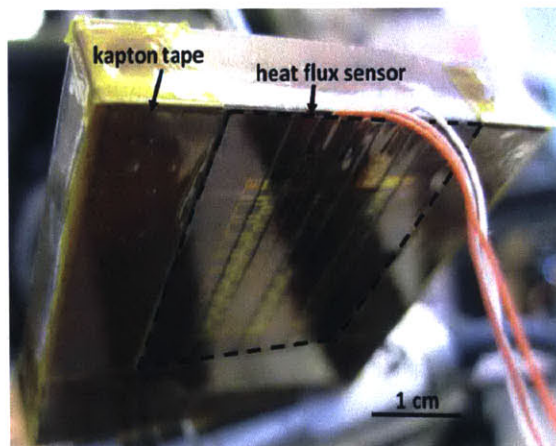


Figure 21: Image of the base of one of the chambers. A thin-film Kapton® heat-flux sensor (Omega HFS-3 or HFS-4) is mounted with double-sided Kapton® tape and then surrounded by layers of single-sided Kapton® tape to form a uniform Kapton® coating. This causes a uniform heat flux to flow across the heat-flux sensor and into the chiller plate below.

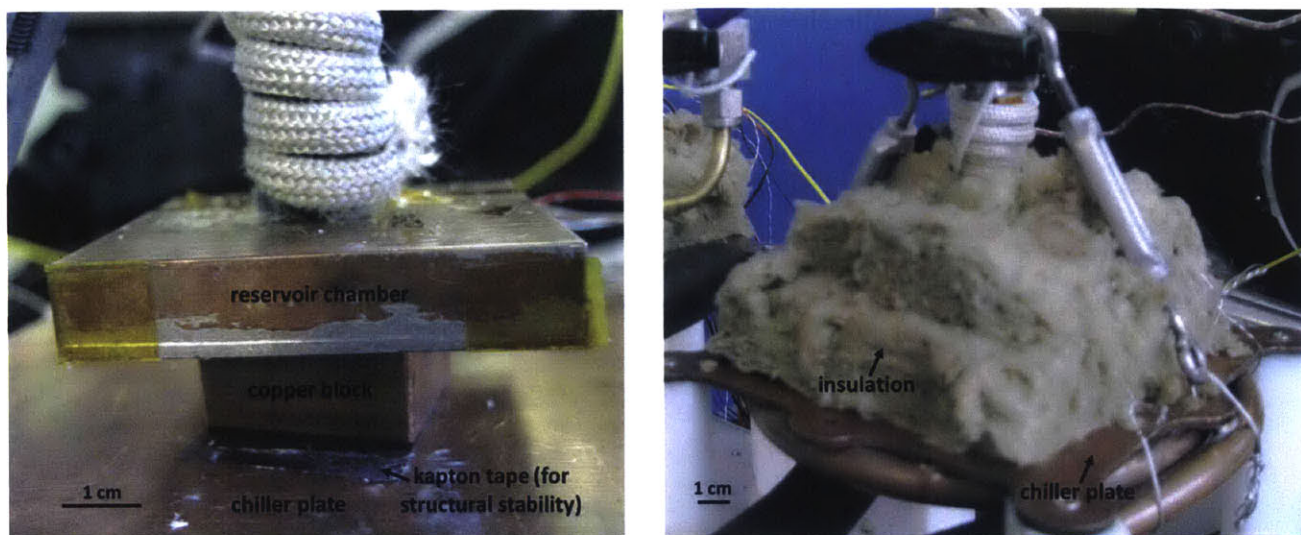


Figure 22: Image of the modified method for mounting the heat flux sensors to the base of the adsorbent and reservoir chambers. This method uses a copper block of the same area as the sensor as the only path for heat transfer from chamber base to chiller plate below, reducing the risk of non-uniform heat flux. The heat flux sensor sits above the directly above the copper block and below the reservoir chamber and is not visible in the image.

it was abandoned in place of another method which proved more reliable. Instead, the sensor was interfaced onto a copper block with the same cross-section as the heat flux sensor and then was sandwiched between the chamber base and chiller plate below. Before running any experiments, insulation is placed around the chamber and block, leaving a gap of air around the block to help with insulation. Figure 22 shows a picture of this configuration applied to the reservoir chamber on the left, and the same configuration with insulation on the right. The heat flux sensor, above the block and below the reservoir base, is not visible in the picture. A conservative calculation was performed to compare the thermal resistances of conduction through the base plate, heat-flux sensor, and copper block to that of natural convection through the air beneath the reservoir chamber. Using a high typical convective heat-transfer coefficient of $10 \text{ W/m}^2\text{K}$ [14], and assuming all heat must travel the longest possible distance through the reservoir base, the convective resistance was around 160 times higher than that of conduction.

Each chiller plate is made from a $3/32''$ thick copper plate with $3/8''$ OD copper tubing shaped into a spiral and soldered to the base (Figure 23). A chiller (Cole-Parmer Polystat 12111-02) is used to route a mixture of water and ethylene glycol at a controlled temperature through the tubing, maintaining a fixed plate temperature. To assist the flow, a pump (Pentair, model 8025-733-256BX) is placed in series with the chiller pump.

Rope heaters (McMaster-Carr 3641K25) are wrapped around the adsorption chamber, the tube above it and below valve C, the tubing between valves B, C, and D including the T junction, and the tube between valve D and the reservoir (see Fig. 24). These heaters

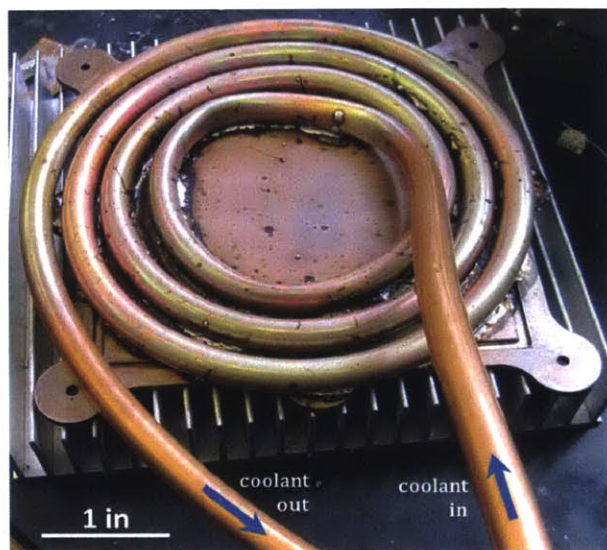


Figure 23: Picture of the underside of one of the chiller plates that is used to keep a constant base temperature beneath the chambers. Copper tubing is formed into a spiral and then soldered to a copper plate, allowing a water/ethylene-glycol coolant mixture originating in a chiller to be routed through.

serve to both heat these components during desorption and to insulate the tubes during adsorption. The chambers are insulated with high temperature glass wool to prevent losses to the ambient and to ensure the majority of the energy leaving/entering the system will pass through the heat flux sensors. Figure 24 is an image of the Dual Chamber Prototype with rope heaters and insulation in place.

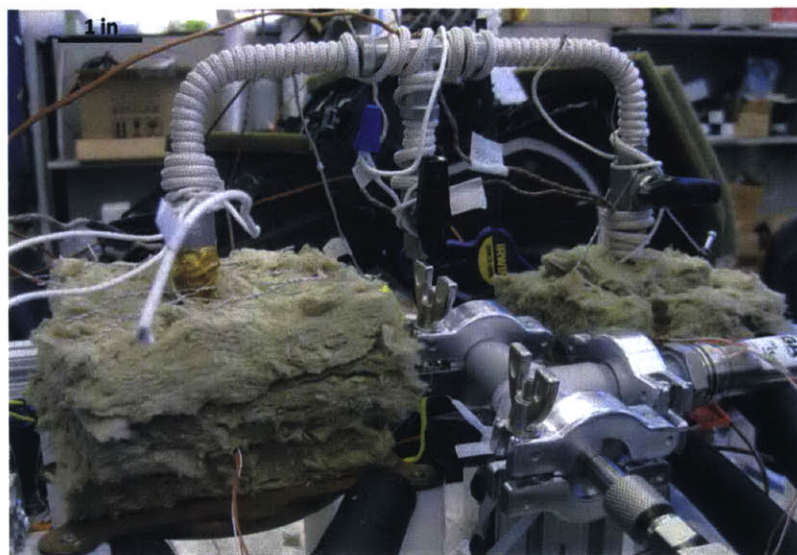


Figure 24: Photo of the Dual Chamber Prototype setup in the lab following installation of insulation and rope heaters.

4.2 Dual Chamber Operating Modes

Dual Chamber Prototype operation can be split into 4 operating modes: preconditioning, leak testing and sensor check, desorption, and adsorption. The first mode is only used once for each set of experiments, making sure that the prototype is filled with the correct amount of liquid to run experiments. The second is to check that the experimental apparatus is operating appropriately during the two experimental modes. The first of these experimental modes, desorption mode is analogous to recharging of a battery, where energy is put into the prototype for storage which will later be released in the second of these, adsorption (discharging) mode, as usable energy. The following sections give quick descriptions of how each of these modes is conducted.

4.2.1 Preconditioning

Preconditioning of the Dual Chamber Prototype is the process of filling the reservoir with a set amount of degassed water and ensuring that all air and noncondensables are removed from the system. To begin, water must be degassed, and the method outlined by H. A. Kariya in Appendix C of his doctoral thesis proved very effective [15]. The filling rig developed for use on the heat pump in that work was still in operation in the lab and was used to degas liquid and fill the reservoir of the Dual Chamber Prototype. A schematic of the filling rig as it was used in this work is shown in Figure 25.

While a more detailed description can be found in [15], a basic overview will be given here. The degassing process is known as freeze-pump-thaw. To begin, water is placed in a metal cylinder, denoted degassing cylinder, which is then submerged in liquid nitrogen, freezing the water. A roughing pump is used to evacuate the gases which are displaced by the formation of the ice crystal structure during the freezing process. Since some gases may remain trapped in the crystal structure, the ice is thawed, re-frozen, and re-evacuated. A total of three freeze-pump-thaw cycles is deemed enough to remove the vast majority of dissolved gases from the liquid.

Once the water is sufficiently degassed, the reservoir section of the prototype (consisting of the reservoir, reservoir valve (valve 7), and tubing attached to that valve) are installed onto the filling rig. Figure 26 shows a photo taken after this step was completed. Next, with valves 1 and 2 closed and all the rest open, the roughing pump and liquid nitrogen trap are used to evacuate all the lines, including the filling burette and the reservoir.

The filling process begins with the filling of the burette. To start, all the valves are closed and heaters are wrapped around the degassing cylinder, raising the temperature of the water inside to around 80°C. The saturation pressure at this temperature is high enough to drive liquid up into the burette. Then, with valve 1 still closed, valves 2 and 3 are opened, allowing the pressure of the heated liquid to force liquid from the base of the degassing cylinder up into the vacuumed filling burette. Then valve 2 can be closed.

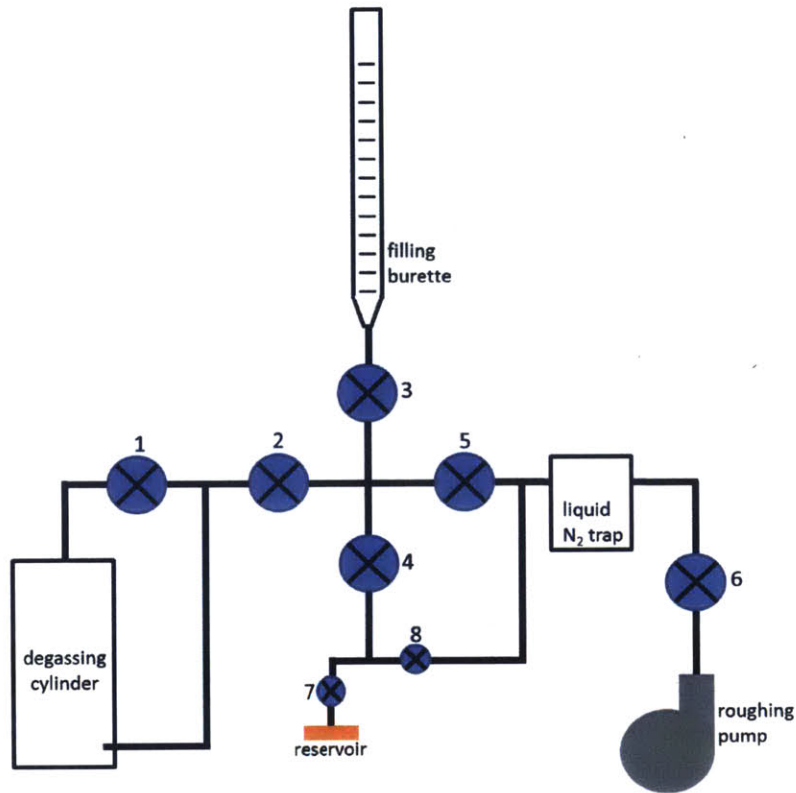


Figure 25: A schematic of the filling rig developed and built by H. A. Kariya for work on a previous heat pipe project [15]. The system allows water inside the degassing cylinder to be degassed using the freeze-pump-thaw method. The water is then filled into the burette, which allows for a controlled amount to be placed into the Dual Chamber Prototype reservoir.

Next, to fill the reservoir, valve 4 is opened, filling the tubing between valves 4, 7, and 8. Then, while monitoring the liquid level in the burette, valve 7 is opened slowly and carefully, letting the desired quantity of liquid into the reservoir. Valve 7 is then closed. Valve 8 and the tubing connected to it, that joins valve 7 to the liquid nitrogen trap, was added to the filling rig to prevent the need to evacuate the cross tubing between valves 2-5 when replacing the reservoir to be refilled. With the addition of this tubing and valve 8, the reservoir can be pumped down using the roughing pump even if the cross tubing is filled with liquid. Since the cross tubing has quite a large volume and it is difficult to remove water from the lines in the filling rig, this addition proved very helpful.

While this filling rig is the most reliable method of filling the reservoir with degassed liquid, an alternative degassing method uses the Dual Chamber Prototype testing system shown in schematic in Fig. 20 (repeated as Fig. 27). The coolant flowing through the chiller plates is a mixture of water and ethylene-glycol with a freezing temperature of about -12°C at ambient pressure, so it was used to cool the reservoir below 0°C , freezing the water inside. This enabled the freeze-pump-thaw method to be performed on the reservoir while it was connected to the testing setup.

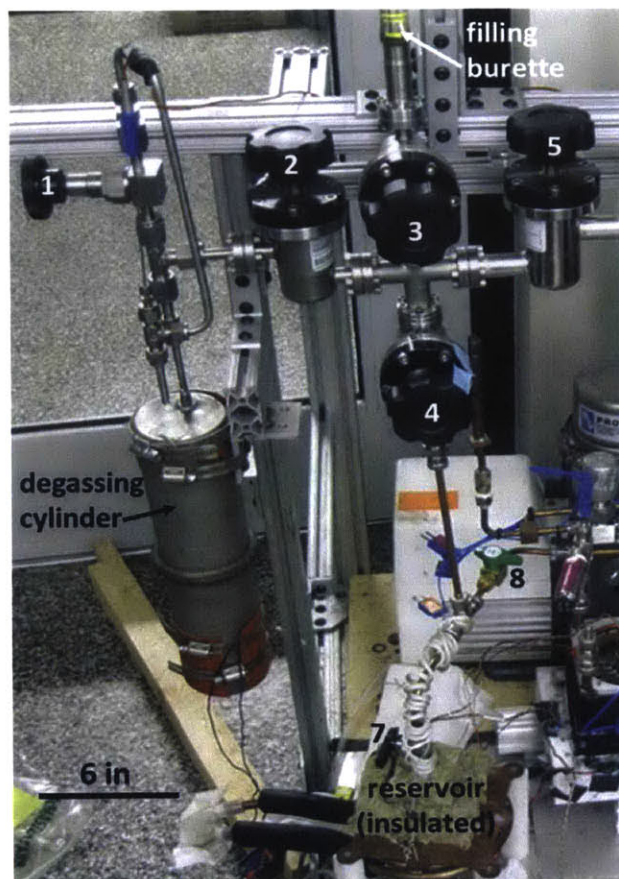


Figure 26: A photo of part of the filling rig. It shows the degassing cylinder on the left, the cross that connects valves 2 through 5 in the center, and the filling burette at the top of the image. The reservoir is attached along with its valve and tubing. Valve 7 on this rig is the same as valve D from Fig. 27.

4.2.2 Leak Testing and Sensor Check

Before collecting any desorption or adsorption data, it is vital to check that the setup is operating as desired and detect any problems that must be resolved. In this mode, the primary goal is to make certain that there are no large leaks in the experimental apparatus and that any air or other undesirable gases that slowly leaked into the lines over time are evacuated. This process is performed in the following way, beginning with valves C and D closed and A and B open (see Fig. 27, a repeat of Fig. 20). The pump is turned on and the lines are evacuated as much as possible, after which valves A and B are closed. The pressure sensor is used to monitor the subsequent pressure, and any leak is located and sealed by tightening connections or applying vacuum grease. Once the section of piping between A and B is deemed leak free (leak rate less than 20 Pa an hour) valve B is opened and the same is done to the total section of piping between valves A, C, and D.

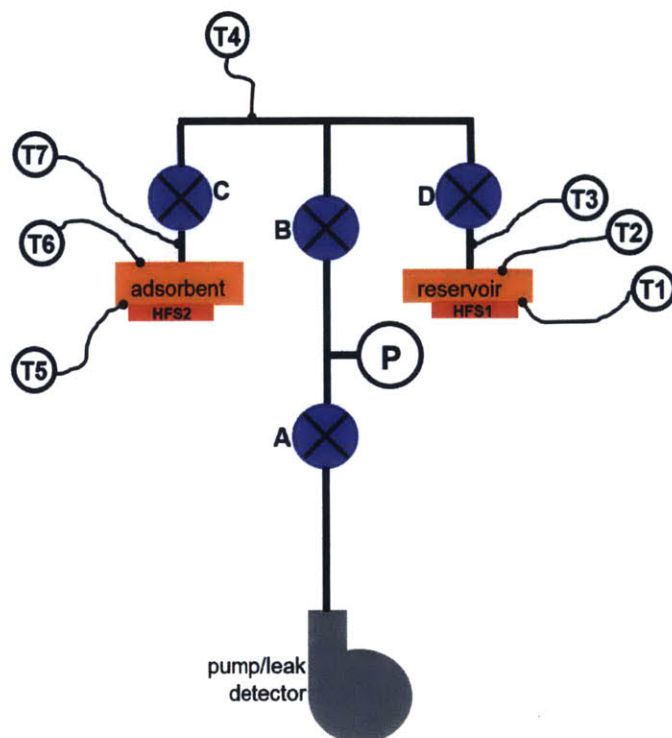


Figure 27: Schematic of the Dual Chamber Prototype setup.

During this process, the sensors are monitored to check that they are all reading physically reasonable values. Any anomalies in the readings are addressed at this time. These checks should be conducted prior to an adsorption or desorption test.

4.2.3 Desorption Mode

Desorption can be carried out in two ways: in the first, a vacuum pump is used to remove the desorbed vapor and keep a low pressure environment to promote further desorption, while in the second a condenser serves this purpose and the condensed vapor is used to refill the system reservoir for future use. Desorption with a vacuum pump is very straight forward. Beginning with valves B, C open and A, D closed, the adsorbent chamber is heated to a high temperature; typically adsorbent base temperature (T4 in Fig. 27) should be greater than 90°C. When the temperatures have reached a high enough value, the vacuum pump is turned on and valve A is opened, removing desorbed vapor. Using two Variac auto-transformers, the rope heater power is adjusted to maintain the desired adsorbent chamber temperatures while the pump is running. After some time, valves A and C are closed and the heaters are turned off, allowing the system to return to equilibrium with the ambient temperature. Both the steady state temperatures and the length of time for heating before closing the valves can be varied to change the desorption conditions.

Desorption with condensation removes vapor from the adsorption bed and deposits it

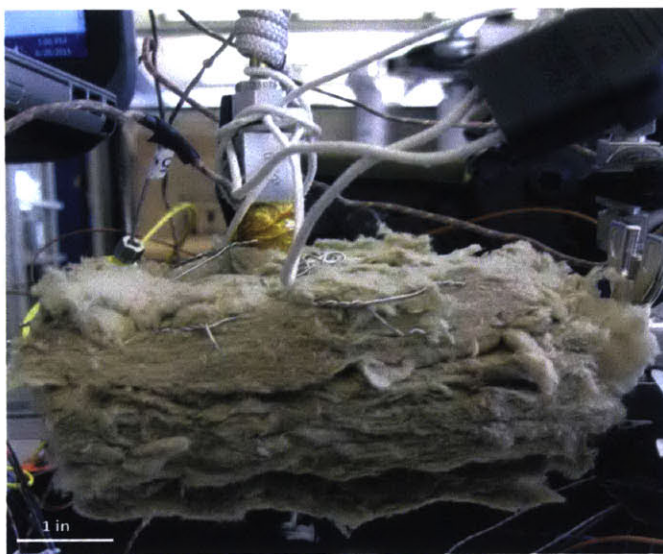


Figure 28: Photo showing the insulation around the adsorbent chamber during the desorption/condensation mode. The chamber is lifted from its chiller plate and another layer of glass wool is secured beneath it, trapping in the heat generated by the rope heaters so that as much as possible goes into the adsorption bed.

in the reservoir where it condenses. This method begins with all four valves closed. The adsorbent chamber is lifted from its chiller plate and insulation is placed beneath it instead to minimize heat loss (see Fig. 28). Then valve C is opened and the rope heaters are turned on to begin heating. By adjusting the two Variacs autotransformers, the rope heater power is controlled such that the hottest temperature in the system is the top of the adsorbent chamber at around 170°C . Equilibrium temperatures are reached so that the tubing thermocouple (T4) reads around 125°C and the tube on top of the reservoir (thermocouple T3) reads near 65°C . Simultaneous to this heating, a chiller is turned on and set to a low value (e.g. 4°C), cooling the plate below the reservoir. The reservoir base thermocouple (T1) will typically read a few degrees above the chiller set temperature.

After some time, a steady state is reached where the system temperatures read as above with a constant power input from both Variacs and the chiller. At this point, the system is ready for condensation, as the high temperature adsorbent has caused desorption, and the high tube temperatures create a high vapor pressure. Valve D is opened, exposing this vapor pressure to the low temperature reservoir (which has a metal foam attached to its base with high surface area), driving the vapor in and causing condensation. Immediately the reading from the reservoir heat-flux sensor (HFS1) will increase to a value significantly higher than its previous steady-state value and then will begin to decay slowly until it returns to that steady-state value. This heat flux can be integrated and multiplied by the reservoir base surface area to give the total energy from condensation.

Once the flux returns to its steady value, valve D is closed, trapping the water inside the reservoir, and the heaters and chiller are shut off, allowing everything to return to

ambient temperature conditions. Note that during this whole process, valve B is closed so the pressure cannot be measured. This was deemed necessary in order to prevent the possibility of condensation in the lines and T-junction between valves A and B, which have a large thermal mass and would be difficult to heat adequately. Finally, valve C is closed and the process is complete.

4.2.4 Adsorption Mode

The adsorption procedure essentially connects the filled reservoir to the dry adsorbent bed, enabling the saturated vapor pressure in the reservoir to drive vapor into the bed. The bed serves a similar purpose to a pump, removing the vapor around it, creating a low pressure zone that perpetuates the process and facilitates evaporation of liquid in the reservoir.

The experimental procedure is simple: first, with valves C and D closed perform a leak check as described in section 4.2.2 and once this is finished make sure that valve A is closed and valve B is open. This allows the pressure in the system to be monitored during adsorption. Place the adsorbent bed back onto its chiller plate (as it was removed during desorption/condensation mode) and run the chiller at 21°C (slightly below ambient temperature so that the chiller plates can be maintained at this constant value during the experiment). Then open valve C and then valve D soon after, recording the heat-flux sensor readings from both the reservoir and adsorbent chambers and monitoring temperatures and pressure until the readings approach their steady-state values and the temperatures return to equilibrium.

5 Testing of the Dual Chamber Prototype

5.1 Predicted Performance

The performance of the Dual Chamber Prototype is governed by the adsorbent sample in the adsorbent chamber. As discussed in Sect. 2.2.2, the power and energy that will be released from the adsorbent chamber in the form of heat depends on the size and physical properties of the adsorbent sample. Additionally, the uptake of the adsorbent determines the amount of liquid that will evaporate, which dictates the cooling performance of the device.

5.1.1 Zeolite MgY Sample

An MgY zeolite sample was placed inside the adsorbent chamber of the Dual Chamber Prototype. It was made by dispersing MgY zeolite in water and submerging the nickel foam in this suspension, allowing the water to evaporate, leaving the zeolite inside the pores of the foam. This process is described in more detail in [16]. The sample is shown in Fig. 29. The sample volume, estimated from the dimensions in the figure, is slightly less than 12 cm^3 . The dry zeolite mass, measured accurately during sample preparation, is 2.755 g.



Figure 29: Picture of the sample of MgY zeolite in nickel foam that was installed into the adsorbent chamber of the Dual Chamber Prototype. Corners were cut off the sample to prevent interference with the fillets on the inside of the chamber.

Thus, the density of the zeolite in the sample is about 230 kg/m^3 , which is typical for MgY samples prepared in this manner. The density is much lower, however, than would be desired to maximize performance of the device, since density can be increased significantly above this value while still meeting reasonable transport metrics. As such, an ongoing effort is underway to create denser MgY zeolite samples for future experiments.

An isotherm measured in the lab for this MgY zeolite is plotted in Fig. 30. This isotherm was taken at 23°C using a dynamic vapor sorption (DVS) analyzer (DVS Vacuum, Surface Measurement Systems Ltd., London, UK). The maximum uptake approaches about 39 weight percent (wt%) as the relative pressure approaches 100%. Thus, for this MgY sample, the theoretical maximum amount of water that can be evaporated in order to be adsorbed is 1.07 grams. This gives a theoretical energy maximum for adsorption heating of 4.4 kJ and a maximum for evaporative cooling of 2.4 kJ from Eqs. 1 and 3 respectively, assuming a value of k_{ads} of 1.8.

These metrics assume full utilization of 39 wt%, which is in reality very difficult to attain. While the dual chamber prototype does usually return to an equilibrium condition at the end of adsorption where the internal pressure is governed by the vapor saturation pressure (corresponding to 100% relative pressure), it is challenging to reduce the partial pressure to approach zero during desorption. Thus, there is inevitably an amount of water left inside the adsorbent at the end of desorption, and this detracts from the amount of vapor that can be adsorbed. In actual system performance, where desorption is performed using condensation,

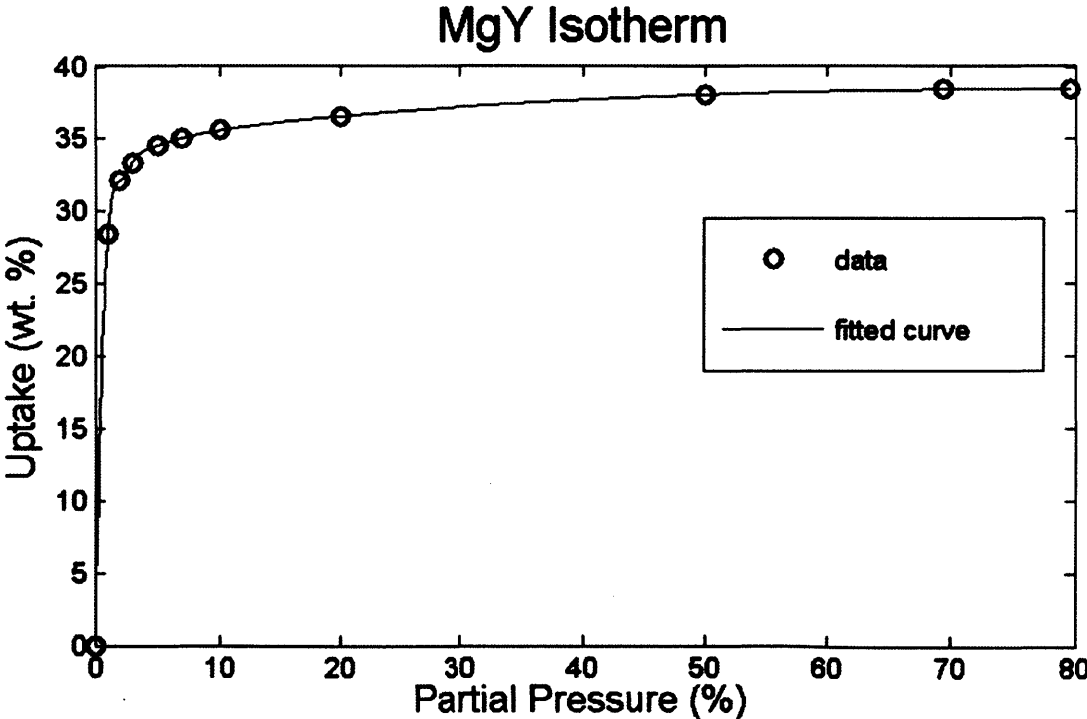


Figure 30: Isotherm for the MgY zeolite used in the sample in Fig. 29, measured at 23°C .

desorbing to less than 15 wt% may be impractical, reducing the theoretical adsorption uptake to around 25 wt%, in turn reducing the maximum energies to 2.8 kJ and 1.6 kJ for heating and cooling respectively.

5.2 Test Results

A series of tests was run using the MgY zeolite sample discussed in Sect. 5.1.1. Since these tests were the first using the Dual Chamber Prototype, their objective was to debug and characterize the prototype. Based on these test results, modifications were made to the prototype and to the experimental procedures. These will improve the system performance and reliability as testing proceeds.

5.2.1 Experiments With Over-filled Reservoir

To begin the first set of experiments, conducted with the MgY zeolite adsorbent bed, the reservoir was filled with more water than that required to saturate the bed. This over-filling of the reservoir allows for several iterations of desorption with a vacuum pump without running out of adsorbate. Each experiment consisted of two parts. The first was a desorption test, where the procedure in Sect. 4.2.3 was followed, using the vacuum pump to remove the desorbed vapor from the system. The second part was an adsorption test, where the procedure of Sect. 4.2.4 was used to measure the heat fluxes, and hence powers, associated with adsorptive heating and evaporative cooling. These tests were run on an early Dual

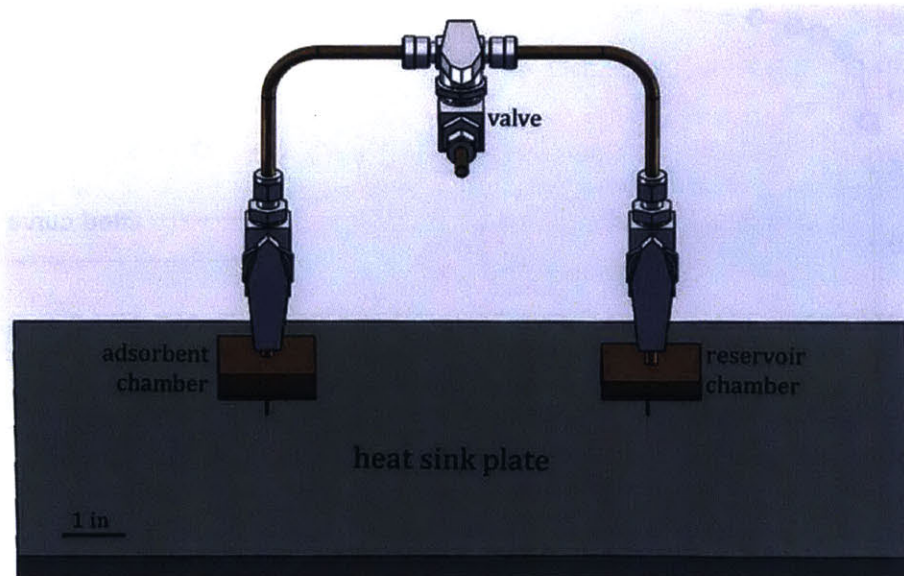


Figure 31: A CAD image of an early design of the Dual Chamber Prototype, where a plate serves as a heat sink below the two chambers.

Chamber Prototype design where, instead of two temperature-controlled chiller plates beneath the system chambers, a large aluminum plate was used as a heat sink. This design is shown in a CAD model in Fig. 31.

Five experiments were run using this prototype design and vacuum pump desorption. A typical plot of temperatures for these desorption tests is shown in Fig. 32, where thermocouples 1-3 and 5-7 from Fig. 27 are recorded. This particular desorption set is from desorption test 4 of this series of experiments. As the plot shows, the adsorbent side is heated and maintained at reasonably high temperatures, while the reservoir side, which has no direct heat input, eventually increases temperature to about 40°C. This increase is due to conduction through the heat sink plate in the initial design, which indicates that the plate was not large enough to really act as a heat sink, and instead allowed some amount of thermal coupling between the two chambers. Although this was not as apparent during adsorption, where the temperatures and heat fluxes are not so extreme, it still indicated that the design should be changed, giving rise to the chiller plates incorporated in the next design iteration.

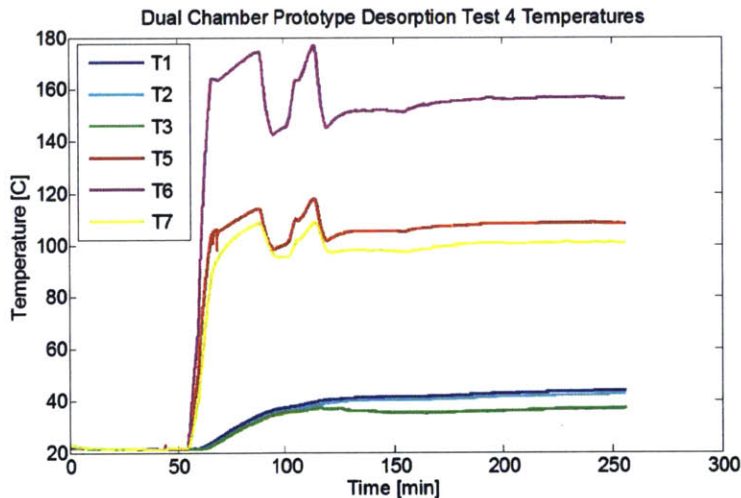


Figure 32: Plot of temperatures from an adsorption with vacuum test. The adsorption bed is in close thermal contact with the adsorbent base and is likely close to the temperature measured by T5. Thermocouple numbers are as shown in Fig. 27.

A typical adsorption test from this set of experiments is shown in the plots in Figs. 33 and 34. Figure 33 plots these same 6 thermocouple readings, and the adsorbent side (T5-T7) clearly rises in temperature while the reservoir side (T1-T3) dips, indicating adsorptive heating and evaporative cooling respectively. The set of plots in Fig. 34 show heating and cooling powers in the top row, determined from the heat-flux sensor readings and the chamber base areas, and heating and cooling energies in the bottom row, calculated by integrating the plots above.

Several aspects of these experimental results were investigated. The first one addressed was the fact that the ratio of heating to cooling energies, which from knowledge of MgY zeolite should be around 1.8, was much higher than expected. The evaporation energy in the

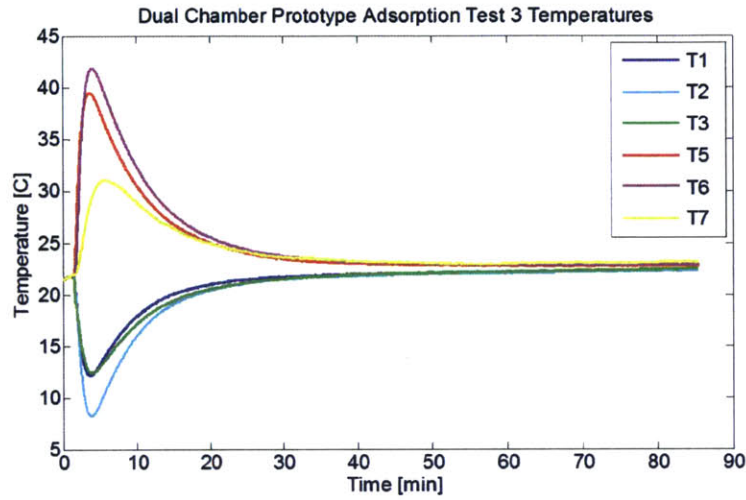


Figure 33: Temperatures measured on the two chambers and tubes above them plotted over the course of adsorption.

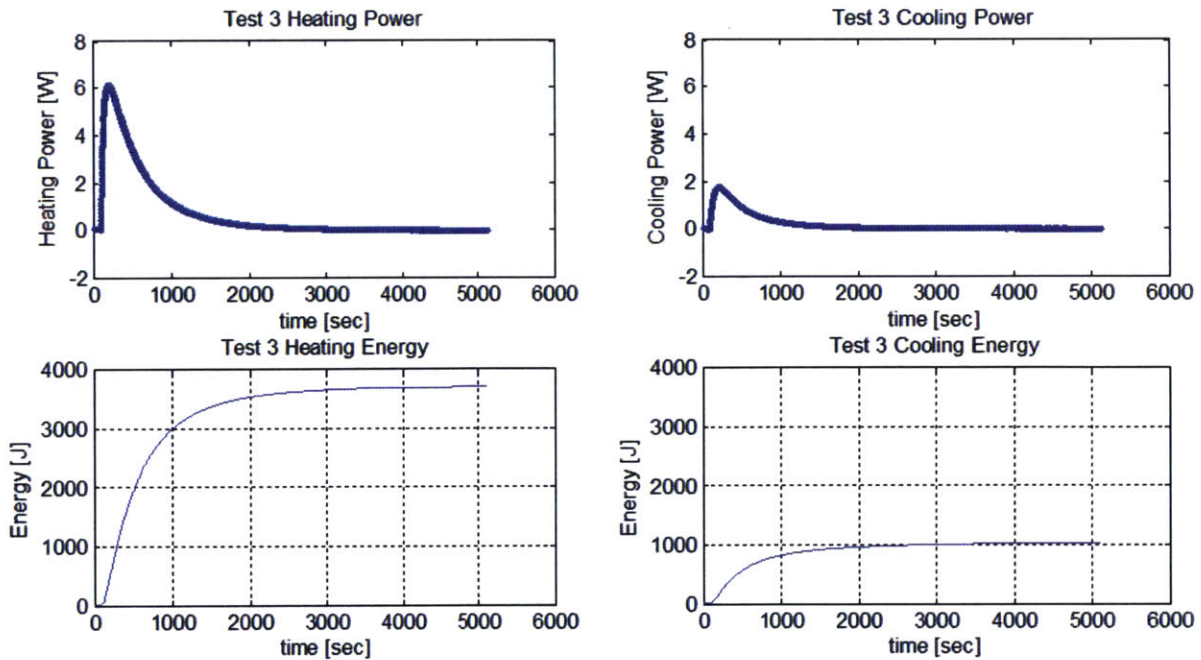


Figure 34: Powers and energies plotted for an adsorption experiment. The top two plots show heating power (left) and cooling power (right) and the bottom two show heating and cooling energies respectively.

reservoir was much lower than it should be, increasing the ratio of heating to cooling energies (k_{ads} from Eq. 5) to upwards of 10 in some cases. The cause of this issue was discovered when investigating some of the adsorption temperature data; at the start of adsorption, the adsorbent chamber tube temperature (T5) dropped significantly before rising, indicating

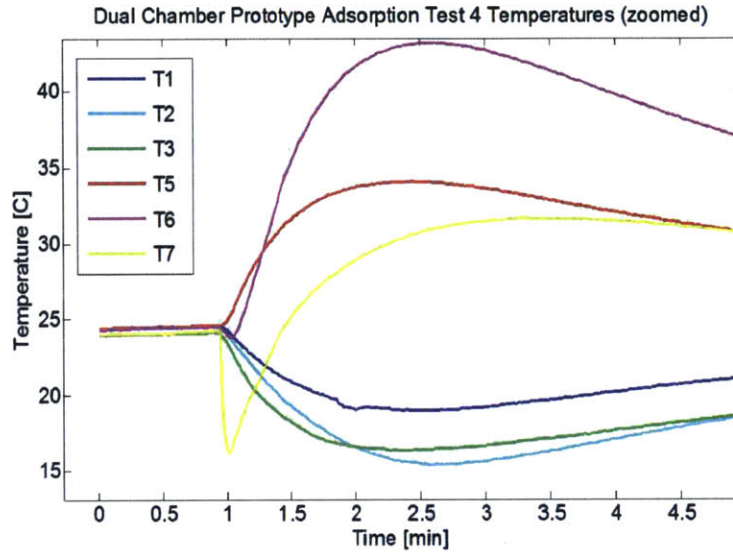


Figure 35: Plot of the temperatures for adsorption test 4. The dip in the adsorbent tube temperature (T7) at around 1 minute indicates liquid is flowing through the prototype tubing.

evaporation was occurring at this location. A good example of this can be seen in the test 4 adsorption temperature data shown in Fig. 35, where the adsorbent tube temperature drops from 23°C to 16°C in a matter of seconds.

This dip in temperature shows that some amount of water in liquid form was able to travel through the tubing from the reservoir to the adsorbent, evaporating on the way or even at the adsorbent surface. This degraded performance in several ways. Since it prevented some amount of evaporation from taking place inside the evaporator, the energy that should have traveled through the reservoir chamber, contributing to cooling energy, was instead taken from another source. At least some of this source was the adsorbent tube and chamber, meaning that the evaporation was extracting energy from these components, subtracting from the heating energy that should have been directed through the adsorbent chamber base through the heat flux sensor. Similarly, if liquid had made it all the way to the adsorbent itself, it must have first evaporated and then been adsorbed, so the net energy released would only have been the difference of adsorption energy and evaporation energy.

A quick calculation indicates why this effect can occur. The maximum tube height in the system is around 15 cm, so the pressure required to move liquid to this height is given by ρgh , where ρ is the liquid density, g is the acceleration of gravity and h is the height. This calculation suggests that a pressure differential of ~ 1.5 kPa will be able to overcome this height obstacle, and since the difference in pressure is often twice this or greater it is likely to occur if liquid is inside the tubing. Thus, the liquid must all be contained within the metal foam in the reservoir. The foam has pores on the order of a hundred microns in diameter, so capillary pressure will act to keep the liquid inside.

In order to guarantee that all liquid goes into the foam and no liquid becomes trapped in the tubing or on top of the foam in the reservoir, the desorption with condensation process from Sect. 4.2.3 was developed. This process creates a high vapor-pressure environment outside the reservoir by heating the adsorbent chamber and all tubing and brings the reservoir base to a very low temperature so that when the reservoir valve is opened vapor is forced into the foam where it condenses.

5.2.2 Experiments With Under-filled Reservoir

Starting with experiment 6, vacuum-pump desorption had removed enough water from the system that there was no longer enough to saturate the bed. A series of tests were performed with this limited amount of water, allowing the desorption/condensation process to be tested and verified. These tests used rope heaters on all the tubing between the two chambers (as shown in Fig. 24) to heat the tubes to a much higher-than-ambient temperature, reducing the possibility of condensation in the tubes. Prior to this set of experiments, the aluminum heat sink plate was replaced by the pair of chiller plates to allow for a very low reservoir base temperature for condensation and create a controlled base temperature on both the reservoir and adsorbent chambers during adsorption.

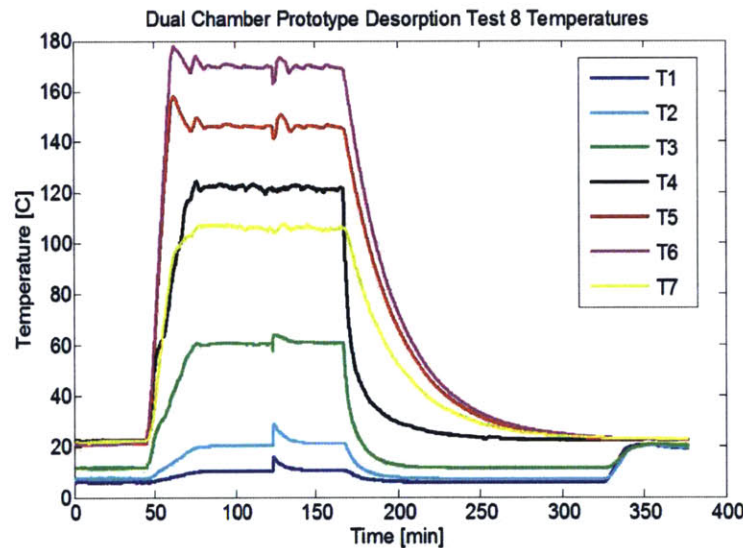


Figure 36: Plot of Dual Chamber Prototype temperatures during a test of desorption with condensation. The increase in temperatures T1-T3 at around 125 minutes is due to vapor condensing in the metal foam inside the reservoir.

The desorption process for this set of experiments follows the desorption with condensation procedure of Section 4.2.3. Typical desorption temperatures are plotted in Fig. 36. In this plot, the reservoir side begins cold, since the chiller was turned on prior to data collection. Then the heaters are turned on and the temperatures are increased and kept at high steady state values. At around 125 minutes, the reservoir valve is opened and the

reservoir temperatures (T1-T3) rise as vapor floods in, releasing sensible heat and then heat of condensation. The temperature rise creates a flux through the reservoir heat-flux sensor as the system returns to its equilibrium temperatures. The condensation energy is determined by integrating the power measured by the reservoir heat-flux sensor, which is shown in Fig. 37.

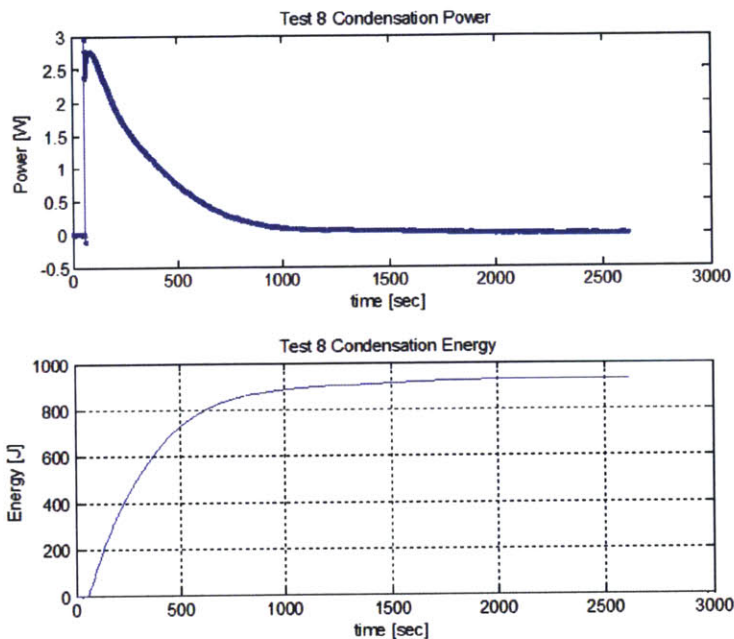


Figure 37: Plot of the power (top) and energy (bottom) measured by the reservoir heat-flux sensor (HFS1) during the condensation process.

The condensation energy gives a good indication of how much water was desorbed in this process. Since the sensible heat contribution is on the order of tens of Joules it can be neglected (or accounted for to some extent) and the energy can be divided by the heat of condensation of water ($h_{fg} = h_g(T_{gas}) - h_f(T_{liq})$) to determine the quantity condensed. In this case, T_{gas} is around 65°C and T_{liq} is around 10°C . At these temperatures, $h_g(65^\circ\text{C}) \approx 2610 \text{ kJ/kg}$ and $h_f(10^\circ\text{C}) \approx 40 \text{ kJ/kg}$ so $h_{fg} \approx 2570 \text{ kJ/kg}$ [11]. Thus, using Eq. 3, the mass of water desorbed for this particular experiment was around 0.35 grams.

Desorption with condensation seemed to solve the problem of liquid traveling through the tubing, yet the experiments here raised another red flag. There was difficulty in repeating the experiments, and the measured value of k_{ads} from the adsorption experiments ranged from 1.0 to 1.7 when tests were rerun at very similar conditions. The fact that the value of k_{ads} is lower than 1.8 is to be expected, since condensation desorption makes it difficult to remove adsorbed molecules from the highest energy sites in the adsorbent microstructure. The RP cannot go as low as with a vacuum pump, meaning higher uptake must remain in the zeolite, as seen on the isotherm (see Fig. 30). However, the lack of repeatability indicated that some aspect of the experimental setup was not consistent, and changed from one experiment to the next.

A likely reason for this was the original heat flux sensor mounting, shown in Figure 21. The idea behind the mounting strategy was to create a uniform layer of Kapton® material beneath the base of each chamber, including the thin-film Kapton® heat-flux sensor, so that a uniform heat flux would flow through the base and through the sensor. It became clear that non-uniformity in the coating layers, even a difference in thickness of a few microns, could create gradients in the heat flow. Since the calculation of power from the heat-flux sensor reading assumes uniformity, this could greatly influence the experimental results. Thus, the new mounting configuration shown in Fig. 22 was devised and implemented to fix this.

5.2.3 Experiments With Refilled Reservoir

A final set of experiments was conducted on the Dual Chamber Prototype. The reservoir was refilled before starting these experiments, so that enough liquid was available to saturate the adsorbent bed. The goal of this set of tests was to repeat the desorption with condensation tests that were performed with an under-filled reservoir, yet this time the capacity of the adsorbent would be able to dictate the energy rather than the amount of liquid. Since the adsorbent sample is well characterized and the amount of liquid in the under-filled reservoir was not quite clear, this would provide a better idea of the expected energy values. This also takes things one step closer to the original goals for the prototype, to test the system level performance with varied parameters.

After refilling the reservoir, it was expected to see higher uptake, with heating energy values that were similar to those seen in the experiments with an overfilled reservoir, and higher cooling values due to the solution of the problem of liquid evaporating outside the reservoir. The experiments did show more reasonable measured values of k_{ads} than in the original experiments, around 1.5, but the total energies were significantly lower than expected. To test the cause of this, desorption with vacuum was repeated with similar conditions to test 4 to

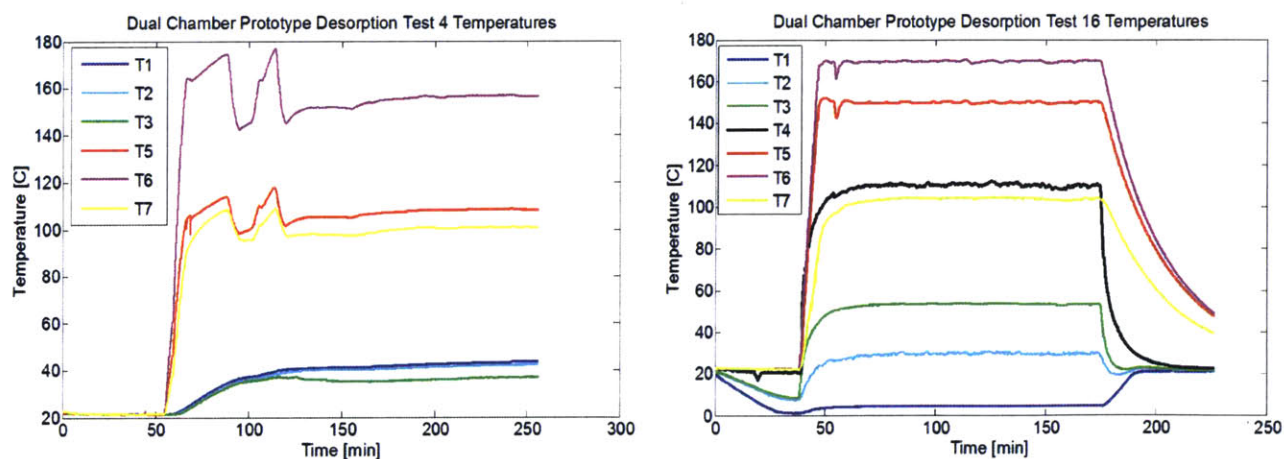


Figure 38: Plots of desorption test 4 (left) and test 16 (right). Both tests were conducted using a vacuum pump and should desorb comparable amounts of water from the adsorption bed.

see if the same adsorption results would follow.

Figure 38 shows the desorption temperatures for test 4 (left) and test 16 (right). Desorption during test 4 brought the adsorbent base temperature to around 110°C for ~3 hours while desorption from test 16 brought it to around 150°C for ~2 hours. Both were run with the vacuum pump. The temperature fluctuations are due to manual temperature control, which was improved with practice between these two experiments. These conditions should be comparable, meaning the adsorbent bed should finish both of these desorption tests with a similar uptake condition (or similar location on the isotherm). The adsorption test that followed desorption 16 is plotted in Fig. 39. The heating energy from adsorption is only around 2.6 kJ, much lower than the theoretical maximum and that of test 4. The two tests are compared in Table 1. The lower adsorption energy indicates that the MgY zeolite material performance had degraded from test 4 to test 16.

Test	Desorption				Adsorption				
	Duration [min]	Adsorbent Chamber Temps [°C]			Duration [min]	Max Cooling Power [W]	Max Heating Power [W]	Cooling Energy [kJ]	Heating Energy [kJ]
		Base (T5)	Top (T6)	Tube (T7)					
4	~ 200	99-117 ± 2.2	142-177 ± 2.2	95-108 ± 2.2	~ 100	1.9 ± 0.2	11.3 ± 1.1	1.0 ± 0.1	4.3 ± 0.4
16	~ 125	142-151 ± 2.2	162-170 ± 2.2	95-104 ± 2.2	~ 115	2.5 ± 0.3	4.5 ± 0.5	1.7 ± 0.2	2.6 ± 0.3

Table 1: Table comparing experiments 4 and 16, which were performed with similar desorption conditions yet yielded very different adsorption results.

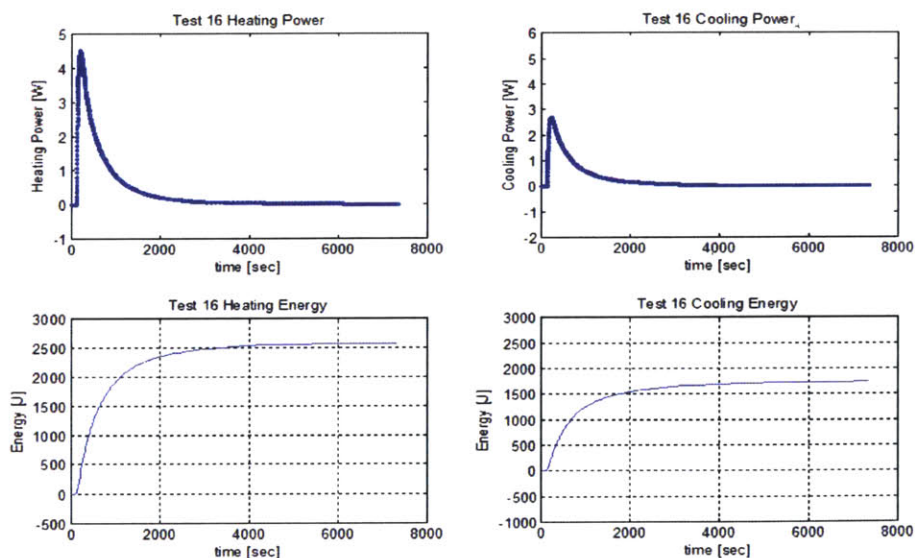


Figure 39: Plots of heating and cooling powers and energies for adsorption test 16, which followed desorption test 16.

5.2.4 MgY Sample Degradation

The cyclic stability of MgY zeolite has been studied [1], and the material should not degrade substantially due to simply adsorption and desorption cycling. However, it was discovered

that the quick temperature ramp rates during the desorption tests could have an effect on the material due to thermal expansion mismatch of molecules that make up the zeolite crystal structure.

The decreased heating performance from adsorption test 4 to test 16 is shown in Table 1. The maximum heating power in test 4 was around 2.5 times the power in test 16, and the heating energy in test 4 was around 1.6 times the energy in test 16. The temperature ramping rate used to test cyclability of MgY zeolite in [1] was 4°C/min, yielding promising results. However, unbeknownst to the author at the time of the experiments, temperature ramp rates higher than ~5°C/min can cause damage to the structure of the zeolite crystals, especially at high vapor pressures, decreasing their ability to adsorb water vapor.

Table 2 shows data collected from a number of the desorption tests. For each of the tests (beginning with test 4 and ending with test 16) the maximum temperature ramping rate occurred for the duration listed, beginning with the adsorbent chamber base at the initial temperature and finishing at the final temperature. The corresponding ramp rate is also listed for each test. In most cases the highest temperature ramping was during heating of the adsorbent chamber, although in test 5 this highest rate appeared during cooling of the chamber.

Test	Duration [min]	Adsorbent Chamber Base Temp [°C]		Approximate Ramp Rate [°C/min]
		Initial	Final	
4	~ 12	24 ± 2.2	104 ± 2.2	6.7
5	~ 6	112 ± 2.2	61 ± 2.2	8.5
8	~ 18	25 ± 2.2	157 ± 2.2	7.3
9	~ 15	25 ± 2.2	160 ± 2.2	9.0
10	~ 7	23 ± 2.2	150 ± 2.2	18.1
11	~ 6	26 ± 2.2	150 ± 2.2	20.7
12	~ 8	23 ± 2.2	151 ± 2.2	15.9
14	~ 12	23 ± 2.2	151 ± 2.2	10.7
16	~ 7	23 ± 2.2	151 ± 2.2	18.3

Table 2: Table of the maximum temperature ramping rate in desorption experiments from test 4 to test 16.

As shown, all of these tests changed the temperature of the adsorbent chamber base (and thus the adsorbent itself) at significantly higher than 5°C/min., with test 11 ramping at more than four times that rate. While no quantifiable degree of degradation as a function of temperature ramping rate has been studied, the significant decrease in heat output from adsorption test 4 to test 16 suggests that the MgY sample was damaged over the course of testing, and future tests will use less extreme ramping conditions to prevent this damage.

6 Conclusions & Future Work

This thesis discusses the development of two small-scale Advanced Thermo-Adsorptive Battery (ATB) prototypes. The Button Cell Prototype was developed primarily to demonstrate the ATB concept for use as a product for small-scale heating and cooling applications. The Dual Chamber Prototype was designed in part to take over the purpose of the Button Cell Prototype but additionally to serve as a testing system for ATB operation in general.

The Dual Chamber Prototype was modified over the course of a series of experiments. Analysis of the data pointed to possible design and experimental procedure flaws which were then rectified. Design modifications included the incorporation of temperature-controlled chiller plates to aid in condensation and control the temperature below the prototype chambers during adsorption, a modified mounting strategy for the heat-flux sensors to reduce variability in the recorded power data, and additional heaters to aid in the desorption process.

It was found that if liquid water, as opposed to water vapor, is able to leave the reservoir of the prototype, the cooling performance decreases significantly. As such, a method for desorption with condensation was developed that drives high-pressure vapor into the porous foam evaporator/condenser inside the reservoir where it condenses. The foam retains liquid, only allowing vapor to flow from the reservoir to the adsorbent bed, a necessity for proper operation. Degradation of the MgY zeolite used to make the adsorbent bed inside the Dual Chamber Prototype was also discovered and attributed to fast temperature ramping during desorption experiments.

The high-ramp-rate degradation of MgY zeolite is a valuable discovery from this prototype, demonstrating the usefulness of such a small testing system. While the zeolite sample inside the prototype will no longer be able to meet high performance metrics, it did serve as a guide for future testing conditions on all systems using MgY zeolite. In the case of the large-scale ATB in development for use in electric cars [2], failure to adequately control the desorption temperature ramp rate could destroy the material in the whole ATB.

As a result of the work presented here, the Dual Chamber Prototype has become a useful tool for further investigations of ATB technology. Desorption conditions, including desorption temperature, time and condensation temperature, can be varied to show their effect on performance. Also of interest is system response as a function of adsorbent sample density, which can be changed by modifying the conditions during sample preparation as well as pressing the sample after it is made. Additionally, changing the adsorbent material to zeolite 13X or any of a number of Metal Organic Frameworks (MOFs) can allow for a direct comparison of how these materials compare to MgY zeolite.

Moving forward, a zeolite 13X sample will first replace the MgY zeolite sample used for the experiments in this work. This sample will be used to run adsorption experiments to verify that the Dual Chamber Prototype adsorption performance matches that shown in component level experiments [9]. Then the desorption time can be varied (maintain bed at

150°C for 1 hr., 2 hrs., 3 hrs.) while desorbing with a vacuum pump to see the effect on the adsorption tests that follow, and then a similar time variation can be performed using condensation instead of a pump. This will allow for a direct comparison of how vacuum pump desorption compares to condensation desorption for zeolite 13X. As a further point of study, the temperature of the reservoir base can be varied during condensation (0°C, 10°C, 20°C) for a given desorption time (2 hrs.).

Following this zeolite 13X sample, a fresh sample of zeolite MgY will be inserted into the adsorbent chamber, and the 13X experiments will be repeated (using appropriate temperature ramping rates). The performance of MgY zeolite can then be accurately characterized and validated based on component level tests [9], and the performance of the two zeolites can be compared directly. This MgY sample can also be used to determine performance degradation as a function of temperature ramping rate. This will help to understand the limits of the material and may be of interest for future adsorbent-based systems that aim to use this zeolite.

Finally, a sample made from a MOF will be installed and compared to the zeolites. The MOF may have a different isotherm shape (as opposed to Type I) and thus may behave very differently from the zeolites. Characterization of these differences could determine if there are operating conditions at which a non-Type-I adsorbent can outperform a Type I, possibly due to higher adsorption energies, lower input energy during desorption, faster desorption time scale or faster adsorption time scale.

As more questions arise regarding ATB system operation, other experiments will doubtless be added to this list, and the Dual Chamber Prototype will continue to serve as a tool to aid the understanding of ATB technology.

References

- [1] X. Li, S. Narayanan, V. K. Michaelis, T. Ong, E. G. Keeler, H. Kim, I. S. McKay, R. G. Griffin, E. N. Wang: *Zeolite Y Adsorbents with High Vapor Uptake capacity and Robust Cycling Stability for Potential Applications in Advanced Adsorption Heat Pumps*. *Microporous and Mesoporous Materials* 201, 151-159, 2015.
- [2] S. Narayanan, X. Li, S. Yang, I. McKay, H. Kim, E. N. Wang: *Design and Optimization of High Performance Adsorption-Based Thermal Battery*. Proc. of the ASME Summer Heat Transfer Conference, 2013.
- [3] S. Narayanan, X. Li, S. Yang, H. Kim, A. Umans, I. S. McKay, E. N. Wang: *Thermal Battery for Portable Climate Control*. *Applied Energy* 149, 104-116, 2015.
- [4] I. S. McKay: *A Monolithically Integrated Thermo-Adsorptive Battery*. S. M. Thesis, MIT Dept. of Mechanical Engineering, 2014.
- [5] N. Srivastava, I. Eames: *A Review of Adsorbents and Adsorbates in Solid-Vapour Adsorption Heat Pump Systems*. *Applied Thermal Engineering* 18, 707-714, 1998.
- [6] B. Coq, G. Delahay, F. Fajulas, B. Neveu, J. Peudpiece, S. Kieger: *Process for the Removal of Gases of Nitrogen Oxides NOX by Selective Catalytic Reduction (SCR) Using Ammonia over Zeolite Catalysts*. U.S. Patent 6221324, 2001.
- [7] D. Ruthven: *Fundamentals of Adsorption Equilibria and Kinetics in Microporous Solids*. *Molecular Sieves* 7, 1-43, 2008.
- [8] J. Kärger, S. Vasenkov, S. M. Auerbach: *Diffusion in zeolites*, in: *Handbook of zeolite catalysts and microporous materials*, S. M. Auerbach, K. A. Carrado, P. K. Dutta, eds., Marcel Dekker, New York, 2002.
- [9] S. Yang, I. McKay, A. Umans, H. Kim, S. Narayanan, H. Furukawa, Y. Zhang, O. M. Yaghi, E. N. Wang: *Realizing the Potential of Metal-Organic Frameworks for Thermal Energy Storage*. Manuscript in preparation, 2015.
- [10] S. Yang, H. Kim, S. Narayanan, I. S. McKay, E. N. Wang: *Dimensionality Effects of Carbon-Based Thermal Additives for Microporous Adsorbents*. *Materials & Design* 85 (In Progress), 520-526, 2015.
- [11] P. J. Linstrom, W. G. Mallard (eds.): *NIST Chemistry WebBook*. NIST Standard Reference Database Number 69, National Institute of Standards and Technology, Gaithersburg MD <<http://webbook.nist.gov>>
- [12] Omega Corporation: *User's Guide: HFS-3, HFS-4 Thin Film Heat Flux Sensors*. Online access, 8/18/2015, <<http://www.omega.com/manuals/manualpdf/M1844.pdf>>
- [13] Omega Corporation: *Revised Thermocouple Reference Tables: Type K*. Online access, 8/18/2015, <<http://www.omega.com/temperature/z/pdf/z204-206.pdf>>

- [14] A. F. Mills: *Heat Transfer*. 1st Edition, Richard D. Irwin, Inc., 1992.
- [15] H. A. Kariya: *Development of an Air-cooled, Loop-type Heat Pipe with Multiple Condensers*. PhD Thesis, MIT Dept. of Mechanical Engineering, 2012.
- [16] H. Kim: *Experimental Characterization of Adsorption and Transport Properties for Advanced Thermo-Adsorptive Batteries*. S. M. Thesis, MIT Dept. of Mechanical Engineering, 2014.